



Research related to the diagnosis of prostate cancer based on machine learning medical images: A review



Xinyi Chen^a, Xiang Liu^{a,*}, Yuke Wu^a, Zhenglei Wang^b, Shuo Hong Wang^c

^a School of Electronic and Electrical Engineering, Shanghai University of Engineering Science, Shanghai 201620, China

^b Department of Medical Imaging, Shanghai Electric Power Hospital, Shanghai 201620, China

^c Department of Molecular and Cellular Biology and Center for Brain Science, Harvard University, Cambridge, MA 02138, USA

ARTICLE INFO

Keywords:

Prostate cancer
Machine learning
Deep learning
MR images
CT images
Ultrasound images
Segmentation
Registration
Detection

ABSTRACT

Background: Prostate cancer is currently the second most prevalent cancer among men. Accurate diagnosis of prostate cancer can provide effective treatment for patients and greatly reduce mortality. The current medical imaging tools for screening prostate cancer are mainly MRI, CT and ultrasound. In the past 20 years, these medical imaging methods have made great progress with machine learning, especially the rise of deep learning has led to a wider application of artificial intelligence in the use of image-assisted diagnosis of prostate cancer.

Method: This review collected medical image processing methods, prostate and prostate cancer on MR images, CT images, and ultrasound images through search engines such as web of science, PubMed, and Google Scholar, including image pre-processing methods, segmentation of prostate gland on medical images, registration between prostate gland on different modal images, detection of prostate cancer lesions on the prostate.

Conclusion: Through these collated papers, it is found that the current research on the diagnosis and staging of prostate cancer using machine learning and deep learning is in its infancy, and most of the existing studies are on the diagnosis of prostate cancer and classification of lesions, and the accuracy is low, with the best results having an accuracy of less than 0.95. There are fewer studies on staging. The research is mainly focused on MR images and much less on CT images, ultrasound images.

Discussion: Machine learning and deep learning combined with medical imaging have a broad application prospect for the diagnosis and staging of prostate cancer, but the research in this area still has more room for development.

1. Introduction

Prostate cancer (PCa) is the second most common cancer, and it is the fifth leading cause of cancer-related death among men. The incidence rates of PCa are 37.5 per 100,000 in developed countries and 11.3 per 100,000 in developing countries, while mortality rates are 8.1 per 100,000 in developed countries and 5.9 per 100,000 in developing countries [1] (See Fig. 2). It is the most commonly diagnosed cancer in men worldwide, with an estimated 1.6 million cases and 0.366 million deaths annually [2,3]. Timely diagnosis and prevention of prostate cancer can greatly improve the survival rate of patients. There are many methods for prostate cancer diagnosis, such as Magnetic Resonance (MR) examination, Computed Tomography (CT) examination, Ultrasound examination and prostate puncture biopsy, among which

Transperineal Template-guided Prostate Biopsy is one of the most effective procedures for the detection of prostate cancer [4,5]. However, as the basis of final diagnosis, biopsy is invasive and associated with pain and risk of bleeding [6]. Therefore, puncture biopsy is only used when there is a high probability that the patient has prostate cancer. Prior to this, the diagnosis of prostate cancer was usually made using medical imaging methods such as MR, CT, and ultrasound (See Figs. 1, 3–6).

The use of medical imaging methods such as MRI, CT, and ultrasound can not only detect prostate cancer, but also diagnose the size, location, and extent of prostate cancer lesions [7]. The traditional method of using medical images to diagnose prostate cancer is to make a judgment call, but the workload of imaging physicians is increasing and there is a mismatch between the demand for work and the number of physicians, so artificial intelligence and imaging images are gradually being

* Corresponding author.

E-mail addresses: c2257873708@163.com (X. Chen), xliu@sues.edu.cn (X. Liu), M325122219@sues.edu.cn (Y. Wu), hanqi_willis@163.com (Z. Wang), wangsh@fas.harvard.edu (S.H. Wang).

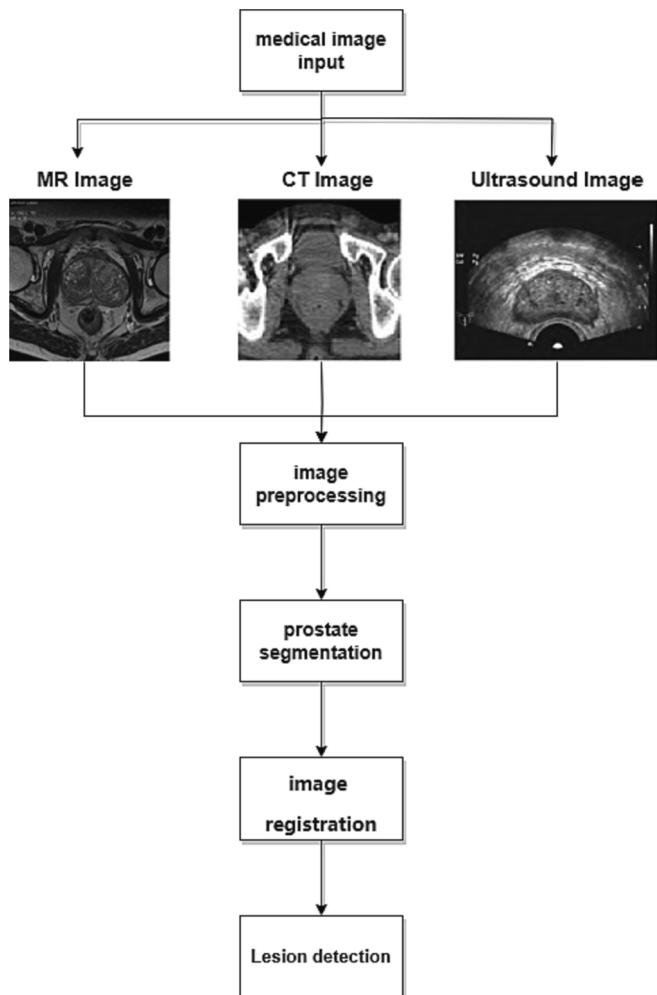


Fig. 1. Medical image processing flow; MR prostate image from [20]; CT prostate image from [21]; TRUS image from [22].

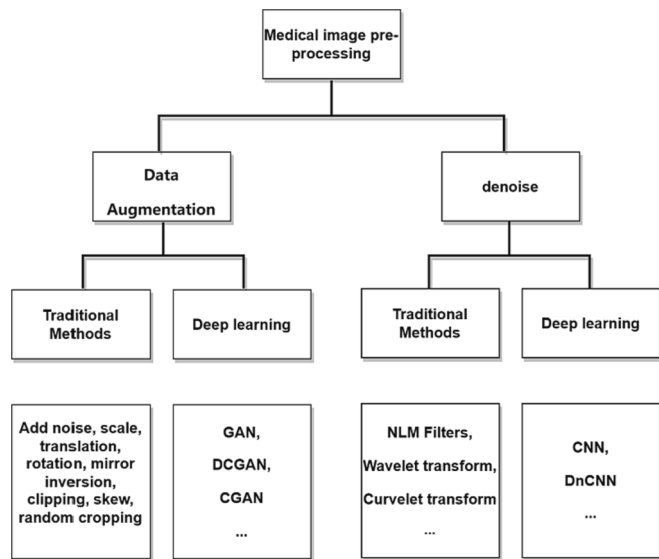


Fig. 3. Pre-processing of medical images.

developed and applied to clinical practice [8]. Artificial intelligence (AI) technologies can perform a wide array of functions, such as aiding in diagnosis generation and therapy selection, making risk predictions and stratifying disease, reducing medical errors, and improving productivity [9–11]. Computer-aided cirrhosis diagnosis systems can contribute to early diagnosis in order to implement target treatment, which can save more people [12]. With the rapid development of imaging technology and the improvement of computer hardware, especially the development of GPU, deep learning has emerged, and artificial intelligence has been more widely used in imaging. [13].

Machine learning is the basis of artificial intelligence, and the core and essence of its research problem is how to use computers to simulate or imitate human learning behavior. Since the late 1980s, with the dramatic increase of computing power, the technology related to machine learning has been flourishing. According to the hierarchy of learning models to classify the development stages of machine learning, it can be roughly divided into two stages: traditional machine learning

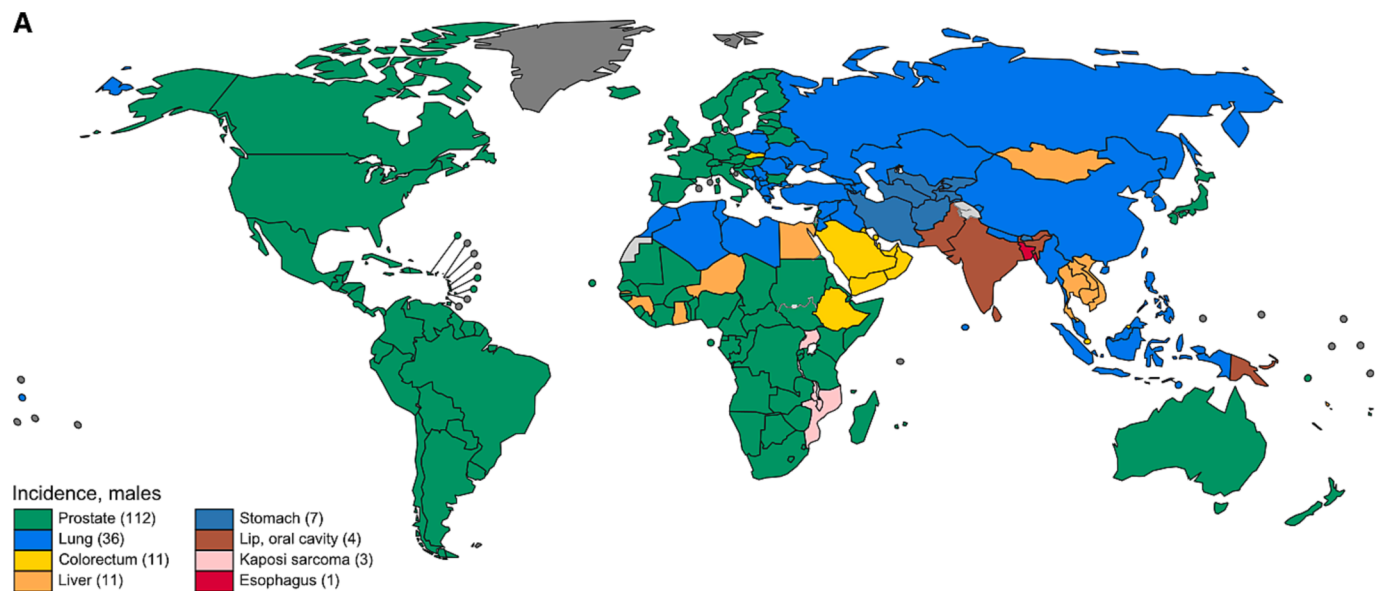


Fig. 2. Most Common Type of Cancer Incidence in 2020 in Each Country Among Men. The numbers of countries represented in each ranking group are included in the legend. .

Source:[1]

and deep learning [14]. In image-based prostate cancer diagnosis, a number of traditional machine learning methods are used, such as support vector machines (SVM) [15], Naive Bayes [16], Logistic regression [17], etc. Many deep learning methods are also used, such as CNN [18], U-Net [19] and other models.

Research on the use of machine learning for diagnosing medical images can be divided into four steps: image detection and pre-processing, prostate segmentation, prostate registration, and detection and classification of prostate cancer lesions. This paper contributes as follows:

1. A comprehensive review of machine learning based techniques for prostate image diagnosis is presented. The latest techniques of image preprocessing, prostate image segmentation, registration between different modal images, detection and classification steps of prostate cancer lesions are discussed specifically with three commonly used images MR, CT, and ultrasound.
2. The performance metrics of each step of traditional machine learning, deep learning on MR images, CT images, and ultrasound images are listed graphically and statistically analyzed.

3. The limitations of the latest deep learning techniques in computer-aided diagnosis of prostate are discussed, the challenges faced and future directions are presented to promote the field.

2. Image pre-processing

Pre-processing of medical images is a very important step in medical image processing. Appropriate pre-processing methods can significantly improve the metrics of image processing results [23]. Pre-processing of medical images includes data enhancement, noise reduction, etc. In this section, the data enhancement and noise reduction of medical images are described.

2.1. Image standardization and normalization

Image normalization and image normalization are essential steps in both traditional machine learning and deep learning. Image normalization is the processing of centering the data by de-meaning, according to the theory of convex optimization and the knowledge related to the probability distribution of the data, the centering of the data conforms to the law of the data distribution, and it is easier to obtain the generalization effect after training. Image normalization is one of the most

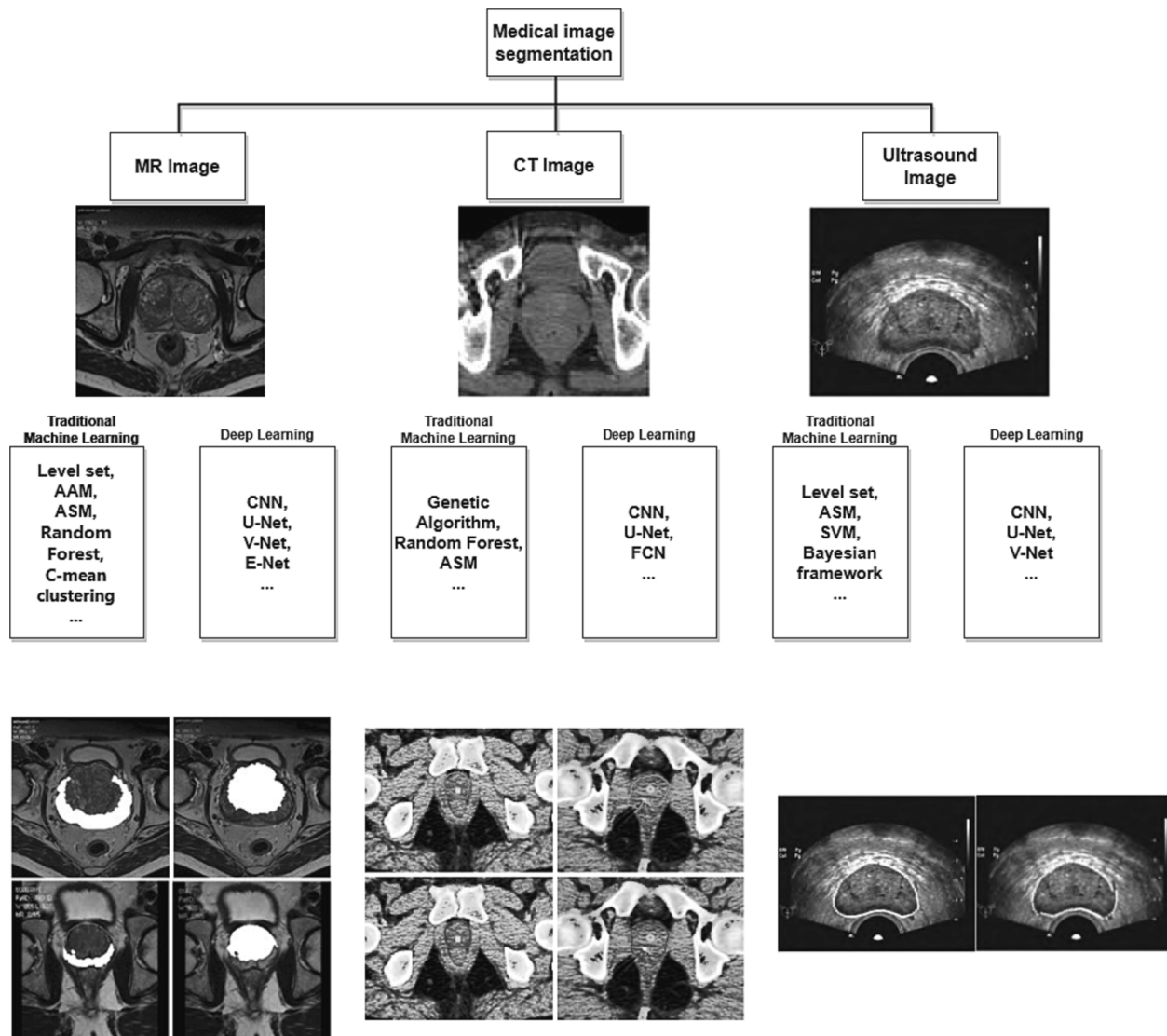


Fig. 4. Prostate segmentation process;MR prostate image from [20]; MR prostate segmentation image from [20];CT prostate image from [85]; CT prostate segmentation image from[86]; TRUS image from [22];TRUS segmentation image from [22].

common methods of image pre-processing, and this is also true for medical images. In image standardization using traditional methods, Feng Yifan et al. [24] used a histogram matching based method to standardize the ultrasound images of pleural effusion after scale normalization of the image set selecting one image as the reference image and its scanning condition as the benchmark condition, and then standardization can be accomplished by turning all the images into images scanned under the benchmark condition. Lee et al. [25] used a deep learning approach to reconstruct and standardize liver CT images based on a GAN network with inputs of FBP, IR, M40, M60, M80, and OPT images, and the output was M80 images, and the reconstructed and standardized images were segmented and compared to the original images, and the DSC for segmentation on the original and the standardized images was 5.40 % respectively –91.27 % and 93.16 %-96.74 % respectively. Comparing the segmentation results, the standardized image has a great improvement in the model performance. Image normalization is also an important component of preprocessing, after normalization, the image feature values can be adjusted to a similar range, which can effectively improve the model training effect. In the field of medical image research, Steffen et al. [26] made a detailed study of normalization methods, using six different normalization methods (setting the mean and standard deviation, histogram matching, percentiles, combining percentiles and histogram matching) on MRI image data of 144 patients from six different centers. percentiles, combining percentiles and histogram matching, fixed window and an auto-encoder with adversarial loss using the imaging parameters) to image normalization, and on the tumor segmentation task and the prediction of the pathological response of locally advanced rectal cancer to neoadjuvant chemoradiotherapy to evaluate the normalization's deep learning Impact. The results of the study show that normalization plays a small role in segmentation, and for the prediction task, the percentile method combined with histogram matching has a better performance in several scenarios. The deep learning approach outperforms the traditional approach in only a few cases. In addition to this, Park et al. [27] for CT images of non-small cell lung cancer used the cubic interpolation method to normalize the voxel size to one-millimeter isovoxels, normalized the reconstructed kernel using the algorithm developed by Gallardo-Estrella et al. and extracted the features of the normalized and the un-normalized maps respectively and constructed a 3-year RFS prediction model of the Random Forest model, in which the pictures after the normalization were carried out had a better performance, especially in the prediction of the patients with adenocarcinoma. In a

prostate related study, DeSilvio et al. [28] used a conditional GAN network to normalize the intensity distribution of prostate MRIs and evaluated the GAN normalization effect using three methods (1. Qualitatively compared the intensity of the GAN normalized images with the intensity distribution of the statistically normalized images 2. Visually inspected the GAN normalized images to ensure that the prostate and other structures were preserved in their 3. quantitatively evaluated the performance of a deep learning holistic nested edge detection (HED) network for identifying prostate cancer on MRI when using raw, statistically normalized and GAN-normalized images), and the results showed that the intensity distributions could be effectively normalized using a conditional GAN. However, the experiment was not tested on other datasets and is not generalizable.

2.2. Data augmentation

Due to the special nature of medical images, the data volume of medical images is usually small. The models trained by these smaller datasets are usually less accurate and prone to overfitting, so data augmentation methods are needed to expand the dataset. The current mainstream approach to data enhancement is based on GAN networks in deep learning, and Generative Adversarial Network (GAN) [29] has been widely used in the field of medical image enhancement because of its excellent image generation performance [30–39]. It also has important applications in the study of prostate cancer. Yu et al. [40] proposed an improved GAN network architecture based on capsule networks, using capsule networks to replace CNNs in GAN networks to generate prostate MR images for classifying prostate cancer images from normal prostate images. The superior performance in image generation was demonstrated by testing on several datasets. Xu et al. [41] used T2W prostate images to train a single natural image GAN (SinGAN) to generate images.

The diffusion model proposed by Ho et al. [42] in 2020 is gradually replacing GAN in the field of image generation due to its excellent performance, and it also has excellent performance in the field of medical image generation. Pinaya et al. [43] used the latent diffusion model to generate synthetic MRI images from high-resolution 3D brain images, judged the fidelity of the generated data by FID, and measured the generation diversity by MS-SSIM and 4-G-R-SSIM, meanwhile, compared with LSGAN, VAE-GAN and other models, in which the FID, MS-SSIM and 4-G-R-SSIM are 0.0076, 0.6555, and 0.3883, respectively, which have high improvement compared with other models.

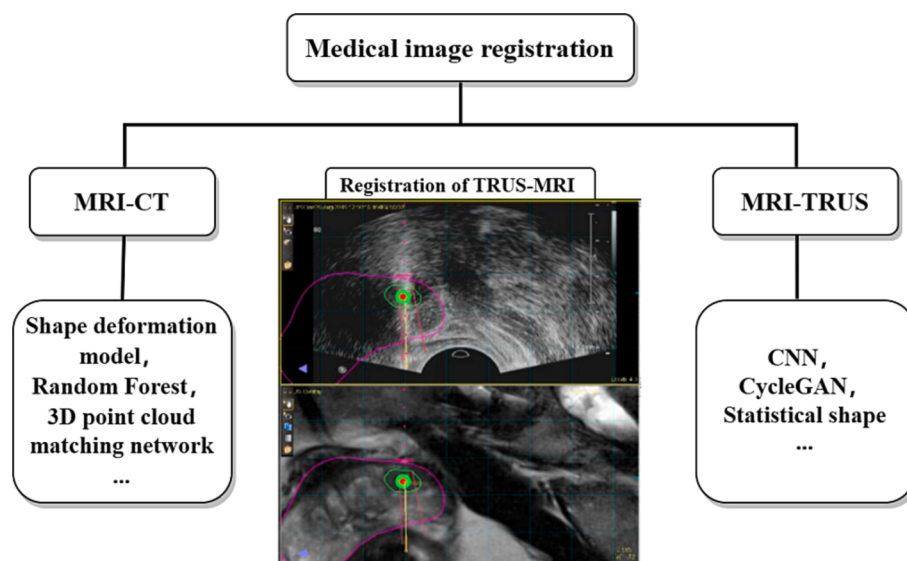


Fig. 5. Registration between different modalities of the prostate; registration image from [131].

Meanwhile, the study makes the synthetic dataset containing 100,000 brain images publicly available to the scientific community. In addition, Gustav et al. [44] trained on multiple types of datasets to generate images and compared with StyleGan-3 on $n = 101,442$ images from the AIROGS challenge dataset to generate fundoscopes with and without glaucoma, ProGAN on $n = 191,027$ images from the CheXpert dataset to generate x-rays with and without cardiac hypertrophy and wGAN comparison of $n = 19,557$ images from the CRCMS dataset to generate histopathology images with and without microsatellite stability. The obtained results Medfusion's FID is 11.63, 30.03 and 17.28 on each dataset, which are better than the GAN network, while Medfusion's fidelity (precision) and diversity (recall) are higher (better).

In addition, the enhancement methods for medical image data include scaling, panning, rotation, specular inversion, cropping, skewing, random cropping, adding noise and other image pre-processing steps on prostate cancer such as [45–48]. While in prostate study, Alkadi et al. [49] expanded the MRI dataset of prostate by adding Gaussian noise, random reflection and panning for training to diagnose prostate cancer. Liu et al. [50] performed in-plane rotation, random cropping and panning to ± 1 pixel for prostate cancer lesions and by these methods 207,144 training samples were obtained for diagnosing prostate cancer.

2.3. Medical image denoising

Image noise reduction research can be divided into traditional methods of noise reduction and deep learning based methods of noise reduction. Among the traditional methods based noise reduction, Non-

Local Means (NLM) filter [51] is the classical one among the traditional noise reduction methods. It can maintain the details of image species as much as possible while noise reduction of the image. Most of the current noise reduction studies have been performed based on NLM filters, such as [52–57], and in prostate studies Kumar et al. [58] used the Hybrid Local and Non-Local Means (HLNLM) filtering model based on NLM to filter the noise present on MR images used to diagnose prostate cancer.

In addition to noise reduction using NLM filter, wavelet transform [59–65], Curvelet transform [66–70], etc. are also used. In a study related to prostate cancer, Gaurav et al. [71] evaluated fifteen filters (Anisotropic, Median, Wiener, Gaussian, Mean, Wavelet, Contourlet, Bilateral, Curvelet, WHMT, NLM, GFOE, LMMSE, CURE-LET and ARF) in prostate image noise reduction studies, where the anisotropic and NLM filters perform well.

Deep learning also has a wide range of applications in noise reduction of medical images [72–77 78–81] and has been studied in prostate cancer, Kaye et al. [82] introduced the concept of guided image filtering based on deep noise reduction neural network (DnCNN) and proposed Guided DnCNN for denoising DW images.

2.4. Discussion

As the application of artificial intelligence in medical imaging becomes more and more widespread, the requirements for data volume and image quality of medical images become higher. Image enhancement and noise reduction techniques can effectively improve the performance of machine learning-based prostate cancer diagnosis.

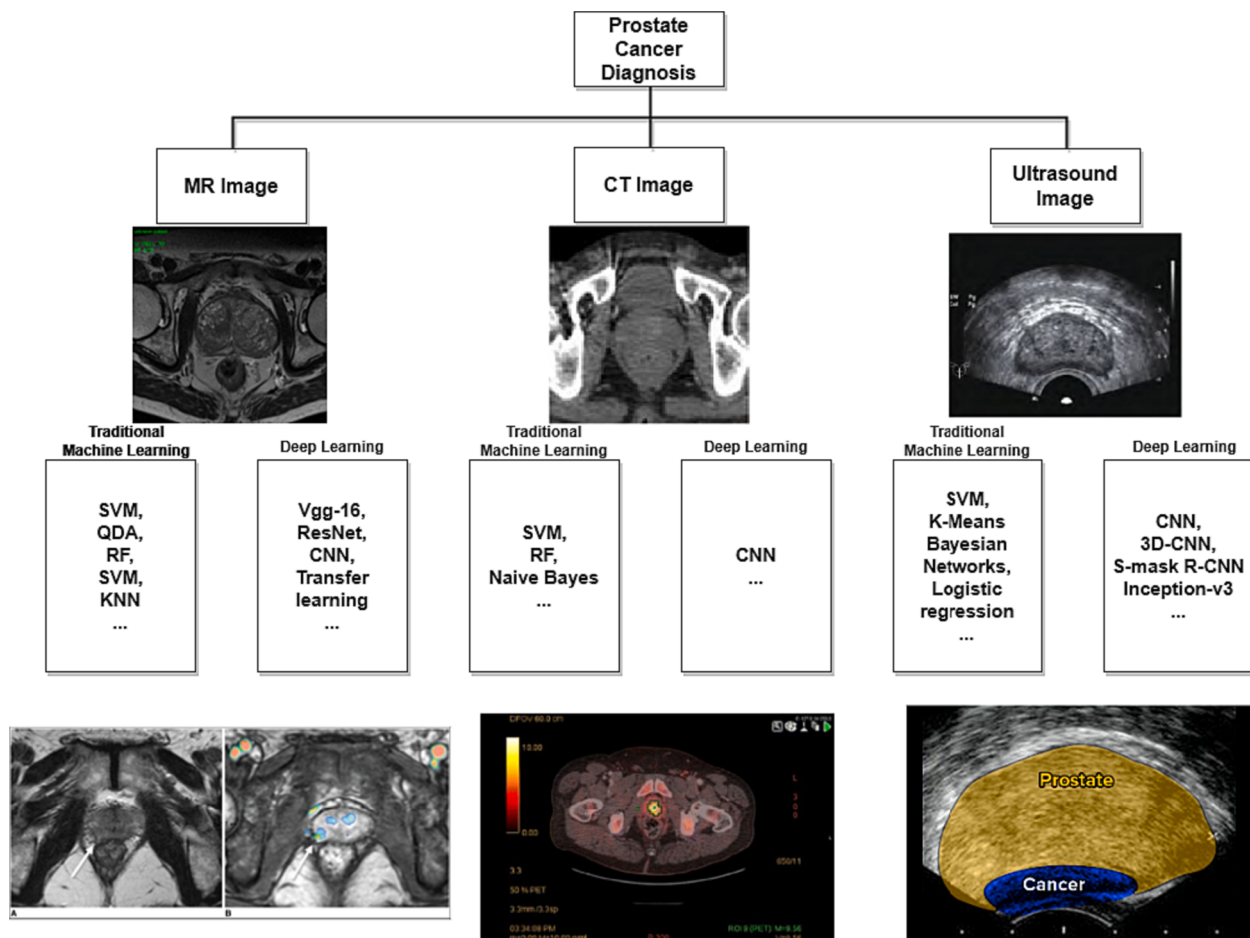


Fig. 6. Detection of lesions on the prostate; Prostate segmentation process; MR prostate image from [20]; CT prostate image from [85]; TRUS image from [22]; MR prostate cancer detection image from [142]; CT prostate cancer detection image from [143].

However, there are few related studies on prostate. Even less research has been done on deep learning applications to prostate image enhancement and noise reduction.

3. Segmentation of the prostate on medical images

Segmentation has an extremely important role in medical image processing [83]. The manual physician segmentation currently used in clinical practice is time-consuming and highly dependent on physician skill and experience, resulting in significant inter- and intra-observer variability. [84] When the prostate is imaged using medical imaging (MRI, CT imaging, ultrasound imaging) methods, the pelvic region is usually imaged, and the resulting image includes the prostate and other organs in the pelvic region. Prostate cancer is an epithelial malignancy that occurs in the prostate gland. Therefore, before using machine learning to diagnose prostate cancer, it is important to accurately segment the prostate gland to exclude other organs or diseases present on other organs from interfering with the diagnosis of prostate cancer. In recent years, machine learning has made great progress in the study of prostate segmentation on MR images, CT images, and ultrasound images, which will be described in this section.

3.1. Segmentation of the prostate on MRI images

For the research of prostate segmentation on MRI, based on the methods used, it can be roughly divided into traditional machine learning-based method segmentation and deep learning-based method segmentation. In the method of shape-based prostate segmentation, Klein et al. [87] segmented the prostate based on a multi-atlas segmentation method, assuming that the accurately labeled images were available as an atlas, and the images in the atlas were registered with the patient images using non-rigid registration. The generated coordinate transformations were applied to the labeled images created by the experts, and the deformed labeled images were combined into a segmented image of the patient. The median Dice Similarity Coefficient (DSC) of the segmentation was 0.85. Level set is an important model in shape-based segmentation methods, and it has excellent performance in segmentation. Based on the level set, Liu et al. [88] used an unsupervised level set approach to find the most suitable ellipse for prostate segmentation using variable ellipses, then used a level set approach to find the prostate boundaries, and finally performed connectivity and morphological analysis, as well as gradient-based correction to subdivide the prostate boundaries. The DSC of this method was 0.91. Robert et al. [89] used a level set based improved Active Appearance Model (AAM) to segment the prostate, using an efficient, intuitive and accurate algorithm to identify those Image Derived Attribute (IDA) that would provide the most accurate segmentation with a segmentation DSC of 0.88 ± 0.05 , with improved speed and accuracy compared to the AAM without the level set. Yan Shiju et al. [90] used the distance regularized level set for the initial segmentation of the prostate region, and based on the gradient information and local grayscale information, the coarse contour was iteratively optimized into a fine contour based on the proposed new energy function. Mahapatra et al. [91] segmented the Volume Of Interest (VOI) using supervoxel segmentation, used images, contextual information, and a second set of forest classifier to create a probabilistic graph of the VOI, and used graph cuts to obtain a final segmentation of the prostate whose mean Dice Metric (DM) of the segmentation was greater than 0.91 on the training set and greater than 0.81 on the test set. Chilali et al. [20] aligned the patient images with the atlas and used C-Means to segment the prostate region, delineating both the prostate and the transition and peripheral zone of the prostate, with segmented Dice of 0.81, 0.70, and 0.62, respectively.

The rise of deep learning has brought a new approach to segmentation. The U-Net segmentation model is always a topic that cannot be bypassed when using networks with deep learning for segmentation tasks. In image segmentation, especially medical image segmentation,

U-Net is undoubtedly one of the most successful methods. Based on the U-Net model, Zhu et al. [92] input the region of interest roughly segmented using the K-Means algorithm into a cascaded U-Net model. The cascaded U-Net model was used to segment the prostate gland with the peripheral zone of the prostate. In the cascaded U-Net network, the prostate was segmented using the U-Net first, and then the peripheral zone was segmented from the already segmented prostate using an identical U-Net. The DSC, False Positive Rate (FPR), and False Negative Rate (FNR) of the segmented prostate were 0.927 ± 0.042 , 0.066 ± 0.077 , and 0.067 ± 0.049 , respectively, and the peripheral zone of the segmented prostate of DSC, FPR, and FNR were $79.3\% \pm 10.4\%$, $17.9\% \pm 10.6\%$, and $15.2\% \pm 12.5\%$, respectively. Also based on the cascade U-Net method, Bardis et al. [93] cascaded three U-Net, where U-Net A was used for localization, and the localized prostate region was input into U-Net B and U-Net C, U-Net B was used to delineate the prostate region, and the delineated prostate region was input into U-Net C, and U-Net C was used to segment the transition zone and The Dice of this method for segmenting the prostate region, transition region, and peripheral region are 0.94, 0.91, and 0.774, respectively. Since the information contained in 3D images is much higher than 2D images, based on this idea, Alexander et al. [94] used 3D images to guide 2D image segmentation. Using 3D images to train the U-Net network and modifying the U-Net downsampling part to enable it to segment 2D images, the Dice of this method for segmenting the prostate was 0.898. (See Table 1)

Although deep learning has the advantages of high segmentation accuracy and fast segmentation in segmentation, it also has the disadvantages of long model training time and high hardware requirements. The transfer learning approach can overcome its disadvantages while retaining its advantages. Motamed et al. [95] used the features learned from the trained model to improve the segmentation results of the new cohort images, applying the idea of transfer learning to improve the U-Net network. The DSC of this method for both prostate and transition zone segmentation could reach 0.80, compared to 0.65 and 0.51 without using migration learning, and the accuracy of this method was greatly improved compared to that without using transfer learning. Based on the full convolutional neural (FCN) model, Tian et al. [96] proposed PSNet to segment the prostate, which is based on a FCN improvement to achieve prostate segmentation by predicting the probability that each voxel belongs to prostate or non-prostate, and the DSC of this network segmentation was 0.85. Also based on the FCN network, Fan Song et al. [21] proposed to segment the prostate with PSP-Net, using the residual structure to construct an effective a priori feature extraction network and develop an optimized curvature, inputting a 2D image obtained from a 3D prostate map slice for training and testing, and the network segmented the prostate with a Dice of 0.913. Renato et al. [97] evaluated the performance of E-Net [98], U-Net [99], and ERF-Net [100] on prostate segmentation. Their DSC on prostate segmentation were 0.9063, 0.8807, 0.8725, respectively. Their DSC on transition zone segmentation were 0.8692, 0.8579, 0.8389, respectively. While each of the three networks has its own advantages and disadvantages, E-Net and U-Net are more accurate than ERF-Net, E-Net converges faster, but the E-Net model has one order of magnitude fewer parameters than the U-Net model. In 3D prostate image segmentation, Liu X. et al. [101] used 3D U-Net to segment the prostate region. The training image was a T2W image manually annotated by an expert, and its DSC for segmenting the peripheral zone, transition zone, central zone, Anterior Fibrous Muscle matrix (AFMS), and urethra were 0.8 ± 0.15 , 0.89 ± 0.07 , 0.52 ± 0.22 , 0.63 ± 0.22 , 0.79 ± 0.16 . Fausto et al. [102] proposed a V-Net network for segmentation of 3D prostate images based on 3D convolutional networks by introducing the residual module and the U-Net framework. The Dice of this network for segmenting the prostate was 0.869 ± 0.033 . Jin et al. [103] proposed 3D PBV-Net based on the V-Net architecture. The input 3D MRI images are pre-processed by bicubic interpolation. The segmentation accuracy of the proposed method on PROMISE 12 [104] [Litjens, 2014 #67] and TPHOH is 0.9765 and 0.9829 respectively, and the Dice is 0.9613 and 0.9765, respectively. (

Table 1

Traditional machine learning-based segmentation methods for prostate MRI images.

Ref	Year	Method	Image Type	Image Dimension	Segmented areas	DSC	DM	HD (mm)	Data source	Sample Sizes			CV
										Train	Val	Test	
[87]	2008	Multi-spectrum segmentation, non-rigid registration	MRI	3D	WG (seminal vesicles)	0.85			PV	38	NM	50	No
[88]	2009	Level set, unsupervised	DWI, ADC	2D	WG	0.91 ± 0.03			PV	10	NM	10	No
[89]	2012	MFLAAM, Level set	T2w	2D	WG	0.88 ± 0.05			PV	86	NM	22	5-fold
[91]	2013	Supervoxel segmentation, Random Forest Graph partitioning	T2W	2D	WG		> 0.91 (test set) > 0.81 (train set)		PROMISE 2012	45	NM	6	10-fold
[20]	2016	C-means clustering	T2w	2D	WG PZ TZ	WG:0.81 PZ:0.70 TZ:0.62			PROMISE 2012;PV	30	NM	35	No
[90]	2021	Distance regularized level set	T2w	2D	WG	0.94 ± 0.01	6.15 ± 0.66		SPIE-AAPM-NCI	203	NM	203	No

Ref = References, DSC = Dice Similarity Coefficient, DM = Dice Metric, HD = Hausdorff Distance, AAM = Active Appearance Model, WG = Whole Gland, TZ = Transition Zone, PZ = Peripheral Zone, PV = Private, CV = Cross-Validation, NM = Not Mentioned, Val = Validation.

Table 2

Deep learning-based segmentation methods for prostate MR images.

Ref	Year	Method	Image Type	Image Dimension	Segmented areas	DSC	Acc	HD (mm)	Data source	Sample Size (patients)			CV
										Train	Val	Test	
[102]	2016	V-Net	MRI	3D	WG	0.869		5.71 ± 1.2	Promise 2012	50	NM	30	No
[96]	2018	PSNet based on CNN	T2w	2D	WG	0.85			PV; ISBI2013; PROMISE12	112	NM	28	5-fold
[21]	2019	PSPNet	MRI	2D	WG		0.9865		PROMISE12	3040 (images)	NM	520 (images)	No
[95]	2019	Transfer learning, U-Net	DWI	2D	WG TZ	WG and PZ > 0.80			PV	8	NM	33	No
[94]	2020	3D image guided U-Net for segmenting 2D images	T2W	2D	WG	0.898			PV	230	NM	57	5-fold
[93]	2021	Cascaded U-Net	T2W	2D	WG PZ TZ	WG:0.94 PZ:0.91 TZ:0.774			PV	145	48	49	No
[97]	2021	U-Net Net ERF-Net	T2W	2D	WG TZ	WG:0.9063(U-Net)0.8807(E-Net)0.8725(ERF-Net) TZ:0.8692(U-Net)0.8579(E-Net)0.8389(ERF-Net)			PROSTATEx	99	NM	105	5-fold
[103]	2021	3D PBV-Net	MRI	3D	WG	0.9613 (PROMISE12) 0.9765 (TPHOH)	0.9765 (PROMISE12) 0.9829 (TPHOH)		PROMISE12; TPHOH	50	NM	30	No
[101]	2022	3D U-Net	T2w	3D	PZ, TZ CZ, AFMS Urethra	PZ:0.8 ± 0.15 TZ:0.89 ± 0.07 CZ:0.52 ± 0.22 AFMS:0.63 ± 0.22 Urethra:0.79 ± 0.16			PV	231	29	28	No

Ref = References, DSC = Dice Similarity Coefficient, WG = Whole Gland, TZ = Transition Zone, PZ = Peripheral Zone, CZ = Central Zone, Acc = Accuracy, FPR = False Positive Rate, FNR = False Negative Rate, HD = Hausdorff Distance, HSD = Hausdorff Surface Distance, AFMS = Anterior Fibrous Muscle matrix; PV = Private, CV = Cross-Validation, NM = Not Mentioned, Val = Validation.

See Table 2)

3.2. Segmentation of the prostate on CT images

Prostate segmentation methods on CT images can also be divided into traditional machine learning-based methods and deep learning methods.

In the traditional machine learning method for prostate segmentation, in the shape-based segmentation method, Artur et al. [105] created a quasi-3D (Active Shape Model) ASM to segment the prostate region, and used a set of continuous 2D organ slice shapes to represent its 3D model. The DSC of the model for prostate segmentation was 0.69–0.76. Li et al. [106] combined the adaptive classifier with the context model, and placed two groups of position adaptive classifiers along the two coordinate directions respectively. The segmented images were used for training, and the different image context information collected at different scales and directions was used for recursive training. The Dice measure of prostate segmentation was 0.908. Commandeur et al. [107] extracted features (e.g. Haarlem features, Gaussian features, gradient features, etc.) from the CT images and assigned them to each voxel, and then used a random forest classifier training to classify each voxel into those belonging to the prostate region and those not belonging to the prostate region. The results obtained after coarse segmentation using random forest were then reconstructed using a spherical harmonic function to obtain the final segmentation results. The DSC of this method was 0.84 ± 0.08 and the HD was 5.67 ± 2.50 mm. Ma et al. [108] used data from prostate patients to train a population model and a patient model based on individual patients. The similarity between the two models was calculated to obtain the applicable population and patient-specific knowledge to calculate the likelihood of a pixel belonging to the prostate region. The DSC of split prostate: 0.872. In the boundary segmentation-based approach, Shao et al. [109] used an algorithm based on regression forest for boundary regression. The nearest prostate boundary point is estimated and voted based on the local image appearance of each image point. Also, the model incorporates an automatic context model to improve the segmentation performance, and its mean sensitivity for segmenting the prostate: 0.84, DSC: 0.85 ± 0.06 , Average Surface Distance (ASD): 2.01 ± 0.81 mm, Mean positive predictive value (PPV): 0.86, false positive ratio (FPR): 0.10. A Genetic Algorithm (GA) was applied to prostate segmentation on CT images of the pelvis by Payel et al. [110]. Shape variability of the prostate gland obtained from manually segmented images was used to form a shape representation of individuals for the randomly generated GA population. Each individual's fitness is assessed based on the texture of the segmentation contour of the region of the prostate it encloses that is considered more suitable than other regions and more likely to be selected to produce the region enclosed by offspring in successive generations of the GA run. The goodness of fit of the segmentation contour to the artificial segmentation contour was 866 (on a scale of 0–1000) and in 3D segmentation, the goodness of fit of the segmentation contour was 951 (on a scale of 0–1000). Maysam et al. [111] segmented the prostate based on the shape and texture of the prostate. The prostate gland is usually spherical in shape, and an inter-subject correspondence between prostate surface points based on spherical coordinates was defined using the center of mass of the prostate as the coordinate origin. This correspondence was used to generate a point distribution model of the prostate shape using principal component analysis. The prostate is segmented based on the texture features of the prostate and non-prostate regions in combination with the input feature. The DSC of segmented prostate: 0.88.(See Table 3)

Deep learning has also been applied to prostate segmentation on CT images. In the method of segmenting the prostate using U-Net, Artur et al. [105] used U-Net to segment the prostate with DSC of segmented prostate: 0.73–0.85. He et al. [112] improved the U-Net to segment the prostate and proposed a network with 2D U-Net architecture to automatically locate the prostate region, segment a picture that completely

Table 3
Traditional machine learning-based segmentation methods for prostate CT images.

Ref	Publication Date	Method	Image Type	Image Dimension	Segmented areas	DSC	FPR	Sen	FFBOT (0–1000)	HD (mm)	Data source	Sample Size(patients)		CV
												Train	Val	Test
[110]	2008	Genetic algorithm	CT	2D	WG	0.908			866		PV	NA	NA	No
[106]	2011	Adaptive classifiers	CT	3D	WG				PV	27	NM	134	No	
[109]	2014	regression forest	CT	2D	WG	0.85 ± 0.06	0.10	0.84	PV	53 (images)	NM	17		4-fold
[107]	2015	Random forest, Spherical harmonic population-based	CT	2D	WG	0.84 ± 0.08			5.67 ± 2.50	PV	100	NM	20	No
[108]	2017	CT	3D	WG	0.872	0.77			PV	74	NM	18		5-fold
[111]	2018	patient-based learning, Shape, texture features, PDM	CT	3D	WG			0.88	PV	23	NM	10	No	
[105]	2021	ASM	CT	2D	WG			0.720	PV	30	NM	9	No	

Ref = References, DSC = Dice Similarity Coefficient, FPR = False Positive Rate, HD = Hausdorff Distance, Sen = Sensitivity, FFBOT = Fitness Function Based On Texture produces a score (0–1000) on Test Images, ASM = Active Shape Model, PDM = Point Distribution Model, WG = Whole Gland, PV = Private, CV = Cross-Validation, NM = Not Mentioned, Val = Validation.

contains the prostate region, and then crop a $128 \times 128 \times 128$ region with the center of the organ. The region is input into the HF-UNet proposed in the paper, which is a multitasking network that can outline the boundary of the prostate while segmenting the prostate. The outlined boundary can overcome the problem of unclear boundary and improve the accuracy of segmentation on CT images. The final prostate segmentation DSC: 0.87, central zone DSC: 0.902 ± 0.015 , and peripheral zone DSC: 0.811 ± 0.028 . Based on the idea of transfer learning and U-Net model to segment the prostate, Ling Tong et al. [86] used MRI images to guide the segmentation of CT images, based on the idea of transfer learning, the P-MRI-UNet model pre-trained using PROMISE 12 dataset, the MRI-UNet model for transfer learning cost experiments, and then the model was transferred into training into CT-MRI-UNet model, and finally migrating it for learning into a CT-UNet network. Finally, the MRI-UNet model and CT-UNet model were migrated and trained into a multimodal U-shaped network for segmenting the prostate region of CT images. The segmented Dice, Precision, and Recall was 0.8959, 0.8873, and 0.9185. Ma et al. [113] used the method of CNN and multi-atlas label fusion to segment the prostate. Firstly, the CNN was used to initially segment the prostate region, and then the multi-atlas label fusion method was used to finely segment the prostate region, and the DSC of the segmented prostate region was 0.868.

Similar to the method proposed by Tong Ling et al. [86] Lei et al. [114] generated synthetic MRI (sMRI) based on CT images using CycleGAN network, trained the network using Deep Attention Fully Convolution Network(DAFCN), prostate contours were outlined on real MRI images and deformed to CT images, added deep attention model to FCN to obtain the most relevant features, added deep supervision to improve feature acquisition capability. Segmented DSC: 0.92 ± 0.09 Sensitivity: 0.92 ± 0.12 Specificity: 0.93 ± 0.06 . Xiong et al. [115] used CNN to extract the region of interest and then used 3D CNN to learn the overall 3D depth features, which were used to differentiate prostate voxels from non-prostate voxels to obtain segmentation results. DSC of segmented prostate: 0.8974, Sensitivity: 0.917 ± 0.039 , PPV: 0.924 ± 0.043 . (See Table 4)

3.3. Segmentation of the prostate on ultrasound images

When using traditional machine learning to segment the prostate on ultrasound images, Sahba et al. [116] used the gradient and the information near the boundary to segment the prostate, used the median filter to slightly deal with the noise on TRUS ultrasound images, and

then used the Top-hat filter and Bottom-hat filter to enhance the boundary of the prostate. The contrast of the bright spaces around the prostate was maximized by top-cap and bottom-cap transformations, and binary images were output using a global threshold. Kalman estimator was used to get the rough prostatic boundary, and gradient and rough estimator information near the boundary were used to get the final segmentation. Compared with manual segmentation, the average distance was 3.3 (Pixels), and the average error was 0.024. To mitigate the disturbance of noise on TRUS images, Yan et al. [117] used only salient contour points for shape estimation, calculated details of shape statistics using a Point Distribution Model (PDM), and estimated shape in advance using a local appearance model. Finally, the discrete deformable model is used to segment the prostate. The average mean absolute distance error was 2.01 ± 1.02 mm. In the method of shape segmentation, Liu Weiping et al. [118] used prior shape model learning and prior shape constraint segmentation, used sign distance function to describe the shape, optimized the square error sum of the two shapes to achieve the rigid registration of the shape, extracted the shape features using the principal component analysis method, and used the Gaussian distribution as the estimation of the deformation parameters. The active contour model based on local Gaussian fitting features was combined with the shape model for prostate image segmentation. Among the twelve patient samples, the DSC of the best segmentation is 0.959886, and the DSC of the worst result is 0.825921. Also using prior shapes, Gong et al. [119] modeled the prostate shape using deformable hyperellipses. The model was fitted to 594 manual prostate contours drawn by five experts. Deformable hyperellipses are used as a prior shape model, and a robust edge detection algorithm is used to generate edge maps for segmentation. The Mean HD of the segmented prostate was 3.42 mm and the Mean Absolute Distance (MAD) was 1.36 mm. Using image features also has an important application in segmentation. In prostate segmentation, Guo et al. [120] used 9 Zernike moments with different order and repetition to extract the texture features of ultrasound images, and retained the amplitude and phase of the moments to obtain 18 feature maps. At the same time, sampling was performed inside and outside the target area of each feature map, and the weight of the feature map was calculated by using the sampling values. Then, the feature map was convolved with the Gaussian operator to calculate its edge detection function. The edge detection functions of all feature maps were multiplied with the corresponding feature map weights, and the sum of the results was the edge detection function of the ultrasound image. Finally, the level set method based on variational function was used to segment

Table 4
Deep learning-based segmentation methods for prostate CT images.

Ref	Year	Method	Image Type	Image Dimension	Segmented areas	DSC	Sen	HD (mm)	PPV	Data source	Sample Size (patients)			CV	
											Train	Val	Test		
[113]	2017	CNN, Multi-atlas label fusion	CT	2D	WG	0.842			PV		74	NM	18	5-fold	
[86]	2018	Transfer learning, U-Net	CT	2D	WG	0.8959			PROMISE12; PV		11	NM	11	2-fold	
[115]	2018	CNN	CT	3D	WG	0.8974	0.917 ± 0.039		PV		120	NM	30	5-fold	
[114]	2020	FCN	CT	2D	WG	0.92 ± 0.09	0.92 ± 0.12	4.38 ± 4.66	PV		49	NM	1	Level-one-out	
[112]	2021	HF-UNet	CT	2D	WG: CZ: PZ	WG:0.87 CZ:0.902 ± 0.015 PZ:0.811 ± 0.028	0.88		0.89	PV		271	NM	68	5-fold
[105]	2021	U-Net	CT	2D	WG	0.796			PV		30	NM	9	No	

Ref = References, DSC = Dice Similarity Coefficient, Sen = Sensitivity, HD = Hausdorff Distance, PPV = Positive Predictive Value, WG = Whole Gland, PZ = Peripheral Zone, CZ = Central Zone, CNN = Convolutional Neural Networks, FCN = Fully Convolutional Neural Networks, PV = Private, CV = Cross-Validation, NM = Not Mentioned, Val = Validation.

the ultrasound image. DSC of prostate segmentation: 0.9636–0.9751. Huang et al. [121] used the DENSE SIFT descriptor to obtain the pixel DENSE SIFT features on the prostate image and input the obtained features into the SVM classifier with positive samples for the prostate region and negative samples for the non-prostate region to obtain the feature segmentation results, which facilitate the selection of the optimal average shape from the established statistical shape models to initialize the shape models. Multiple shape models were created, and the optimal shape model was selected as the initial segmentation profile from the established shape models. Multi-resolution segmentation was used for the final segmentation, and the segmented DSC: 0.9552, MAD: 0.5016 mm, HD: 1.6829 mm, specificity: 0.9964, sensitivity: 0.9451.

A priori and a posteriori is important idea in machine learning, has important application in the segmentation of prostate. The idea of prior is reflected in the prostate segmentation method of Gong, Liu [118], Huang et al. [121], and the idea of posterior is reflected in Ghose et al. [122], using the Bayesian framework to determine the posterior probability of the pixel is prostrate, adjusting multiple statistical models of shape and texture prior to combine the posterior probability of the prostate region for training, initialization and propagation of the parameter model, One of the average models is selected to segment the prostate according to the fitting error of the posterior probability. DSC: 0.97 ± 0.01 , MAD: 0.49 ± 0.20 mm. In using an unsupervised approach, Richard et al. [123] used clustering to automatically segment the prostate, extracting image features using Laws texture energy measures, labeling pixels using the most likely class for each pixel to classify them using a feature space clustering process based on four feature images to determine the number of classes and define class means and variances. The algorithm is computationally intensive and the number of classes generated is not completely predictable.(See Table 5)

When using deep learning methods to segment the prostate on ultrasound images, Lei et al. [124] used a multi-way deep supervised V-Net to segment the prostate. The images are pre-processed using bias correction and de-speckling to remove noise. A multi-way-based deep learning network is trained using images in the transverse, sagittal, and coronal planes. Filtering is performed using a Gaussian filter, a mean filter, and a median filter. The filtered images are used along with the original images to form 4-channel image data or multi-validation-based data. Using the 3D patch-based V-Net26 architecture, 3D deep supervision is added to address the optimization difficulties in training deep networks with limited training data. DSC of the network segmented prostate: 0.92 ± 0.03 , HD: 3.94 ± 1.55 mm, MSD: 0.60 ± 0.23 mm, and residual MSD: 0.90 ± 0.38 mm. To solve the problem of noise interference in TRUS images, Wang et al. [125] added Deep Attentional Features (DAF) modules to the CNN, generated DAF at each layer according to the principle of attention mechanism, obtained segmentation maps from the DAF of each layer, and finally obtained the segmentation maps of each individual layer by Finally, the segmentation result is obtained by averaging the segmentation maps of each individual layer. Dice of segmented prostate: 0.9527, Average Distance of Boundaries: 4.5734 mm, Conformity Coefficient: 0.9000, Jaccard: 0.9369, Recall: 0.9698. Similarly, deep attention mechanism was added to the network, Wang et al. [126] the following year proposed a new network applied for segmenting 3D TRUS images, developed a 3D attention-guided network equipped with an attention module in the network by exploiting the spatial context of deep and shallow layers, and used the attention mechanism to selectively refine the features of each individual layer by using multi-level features integrated from different layers. The non-prostate noise in the shallow layers of CNN is suppressed and more prostate details are added to the features in the deep layers to improve the classification. Orlando et al. [127] based a 2D U-Net network to segment 3D TRUS images using 2D images that have been labeled for acquisition in random axial, sagittal, coronal, radial, and tilted image planes to train the 2D U-Net network, and to segment the prostate in 3D TRUS, the 3D prostate image is sliced radially and the sliced image is

Table 5 Traditional machine learning-based segmentation methods for prostate Ultrasound images.

Ref	Publication Date	Method	Image Type	Image Dimension	Segmented areas	DSC	HD (mm)	MAD (mm)	Sp	Area error %	Data source			CV
											Train	Val	Test	
[123]	1996	Clustering algorithm	Ultrasound	2D	WG						PV	NM	NM	No
[119]	2004	Shape model	TRUS	2D	WG						PV	16	NM	No
[116]	2005	Kalman estimator	TRUS	2D	WG						PV	19	NM	No
[117]	2010	ASM	TRUS	2D	WG						PV	19	NM	No
[122]	2011	The Bayesian framework	TRUS	2D	WG						PV	22	NM	1 Level-one-out
[118]	2012	Level set	TRUS	2D	WG	0.825921–0.959886					PV	11	NM	1 Level-one-out
[121]	2015	SVM	TRUS	2D	WG	0.9552	1.6829	0.5016	0.9964		PV	30	NM	30
[120]	2015	Zernike moment, Level set	TRUS	2D	WG	0.9636–0.9751					PV	5	NM	5

Ref = References,DSC = Dice Similarity Coefficient, HD = Hausdorff Distance, MAD = Mean Absolute Distance, Sp = Specificity, TRUS = Trans-Rectal Ultrasound, SVM = Active Shape Model, SVM = Support Vector Machines, WG = Whole Gland, PV = Private, CV = Cross-Validation, NM = Not Mentioned, Val = Validation.

input to the trained 2D U-Net to segment the prostate, and then remodel the 3D image to obtain the final segmentation profile after the segmentation is completed. The segmentation DSC: 0.941, Recall: 0.96, Precision: 0.932, area\volume percent difference: 0.0578, MSD: 0.89 mm, HD: 2.89 mm. Chu et al. [128] used the yolo5 detection algorithm to localize the prostate gland. After localization, the prostate shape was described using statistical prior knowledge and the prostate was modeled using a point distribution model. The method segmented the prostate with Dice: 0.9482, Precision: 0.9505, and recall: 0.9647. (See Table 6)

3.4. Discussion

The use of machine learning segmentation can effectively improve the efficiency of diagnosis and reduce the workload of physicians. With the improvement of traditional machine learning methods and the rise of deep learning, the segmentation accuracy of the prostate is getting higher and higher, but there is still room for improvement. At the same time, there are fewer studies on segmentation of the upper part of the prostate, and the accuracy is low, and most studies on segmentation of the partition have a DSC of about 0.8. Deep learning has better performance on segmentation than traditional machine learning.

4. Prostate image registration

4.1. Image registration

Image registration is an important part of medical image processing. Registration is a fundamental task in image processing used to match two or more pictures taken [129]. Medical image registration is the search for a spatial transformation (or series of transformations) for a medical image to achieve spatial agreement with corresponding points on another medical image. This agreement means that the same anatomical point on the human body has the same spatial position on the two matched images. The result of the registration should be such that all anatomical points on the two images, or at least all points of diagnostic significance and surgical interest, are matched [130]. At present, the medical diagnosis of prostate mainly uses MR Images, CT images and ultrasound images, and the registration research is also to study the registration between the three. In this section, we discuss the registration between these three types of images.

In the research of MRI and TRUS image registration method, Cong et al. [132] extracted the TRUS prostate contour and MR Prostate contour Shape Context features manually, and then performed discrete sampling of the contour of the TRUS prostate image segmented by the automatic segmentation algorithm and the manually segmented prostate image. The improved KM algorithm is used for contour matching,

and the thin plate spline registration method with anisotropic error is used for the final image registration. The DSC of nine groups of registration results is greater than 0.98. To register the prostate deformed by compression during surgery, Mohamed et al. [133] used a biomechanical model to simulate the prostate deformation, used principal component analysis to extract the main deformation for training the model, and used least squares fitting to construct the deformed prostate shape from CT or MRI. Hu et al. [134] also used a biomechanical model to obtain prostate deformation data, used a finite element simulation of the ability of a statistical shape/motion model trained to predict and compensate for the motion sources of the gland, and used a statistical motion model to perform registration. The average final target registration error (TRE) (based on anatomical landmarks) of this method was 1.8 mm.

In using deep learning for MRI-TRUS image registration, Hu et al. [135] used a weakly supervised CNN for image registration using high-level correspondence information contained in anatomical labels to infer voxel-level transformations. The median target registration error was 3.6 mm for the marked ventricle and 0.87 for the median Dice of the prostate. Yan et al. [136] proposed an adversarial image registration framework that allows simultaneous image registration and evaluation of image registration results by training two deep neural networks, a generator and a discriminator, in an adversarial manner. The TRE was 3.48 mm. Zeng et al. [137] used a 2D CNN to align MRI-TRUS prostate images using affine registration for initialization of the registration and then a 3D UNET-like for non-rigid registration. TRE: 2.53 ± 1.39 mm, mean Dice loss: 0.91 ± 0.02 , MSD: 0.88 mm, HD: 4.41 mm. Chen et al. [138] used two 3DV-Nets to segment prostate gland in MR And ultrasound images based on segmentation registration method, and used two networks to generate prostate probability graphs from MR And ultrasound images as weak supervision labels in the subsequent registration process. The 3D UNET-like was used for registration. Mean DSC: 0.87 ± 0.05 , center-of-mass distance: 1.70 ± 0.89 mm, HD: 7.21 ± 2.07 mm, averaged symmetric surface distance: 1.61 ± 0.64 mm. Yang et al. [139] registered using a CNN for MR Prostate, TRUS for TRUS prostate segmentation and a non-rigid registration framework based on the composition of point cloud networks for fast 3D point cloud matching. DSC: 0.94 ± 0.02 , MSD: 0.90 ± 0.23 mm, HD: 2.96 ± 1.00 mm, TRE: 1.57 ± 0.77 mm.

In MRI image to CT image registration, Shafai-Erfani et al. [140] used a random forest based on context model training to generate CT images for MR Images in the training set. Lei et al. [114] used a CycleGAN network to generate synthetic MRI (sMRI) based on CT images. Fu et al. [141] proposed a registration framework considering MR Deformation into CBCT biomechanical constraints, and the framework contains a segmentation CNN for segmenting MR and CBCT prostate and a 3D point cloud matching network for registration. DSC: 0.93 ± 0.01 ,

Table 6
Deep learning-based segmentation methods for prostate Ultrasonics image.

Ref	Publication Date	Method	Image Type	Image Dimension	Segmented areas	DSC	HD (mm)	Pre	Re	Data source	Sample Size(patients)	CV		
										Train	Val	Test		
[125]	2018	CNN, attention Mechanism	TRUS	2D	WG	0.9527		0.9698	PV	10	NM	7	No	
[126]	2019	CNN, attention Mechanism	TRUS	3D	WG	0.90 ± 0.03	8.37 ± 2.52	0.90 ± 0.06	0.91 ± 0.04	PV	30	NM	10	No
[124]	2019	V-Net	TRUS	3D	WG	0.92 ± 0.03	3.94 ± 1.55		PV	43	NM	1	Level-one-out	
[127]	2020	U-Net	TRUS	3D	WG	0.941	2.89	0.932	0.96	PV	100 (images)	NM	20 (images)	No
[128]	2023	YOLOv5, PDM	TRUS	2D	WG	0.9482		0.9505	0.9647	PV	100	NM	20	No

Ref = References, DSC = Dice Similarity Coefficient, HD = Hausdorff Distance, Pre = Precision, Re = Recall, PDM = Point Distribution Model, CNN = Convolutional neural netw, PV = Private, CV = Cross-ValidationL, NM = Not Mentioned, Val = Validation.

Table 7

Prostate image registration with machine learning and deep learning.

Ref	Publication Date	Method	Registering images	DSC	HD (mm)	TRE (mm)	MSD (mm)	MEE
[133]	2002	Shape deformation model	MRI/CT-TRUS					<0.267
[134]	2011	Statistical shape	MRI-TRUS			1.8		
[135]	2018	Weakly-Supervised Image Registration Framework	MRI-TRUS	0.87				
[136]	2018	adversarial image registration (AIR) framework	MRI-TRUS			3.48		
[140]	2019	Random forest	MRI-CT					
[137]	2020	3D UNET-like network	MRI-TRUS		4.41	2.53 ± 1.39	0.88	
[139]	2020	biomechanically constrained deep learning	MRI-TRUS	0.94 ± 0.02	2.96 ± 1.00	1.57 ± 0.77	0.90 ± 0.23	
[114]	2020	CycleGAN	CT-MRI					
[132]	2020	AAM, Random forest Thin Plate	MRI-TRUS	> 0.98				
[138]	2021	segmentation-based registration framework	MRI-TRUS	0.87 ± 0.05	7.21 ± 2.07			
[141]	2021	3D point-cloud matching network	MRI-CBCT	0.93 ± 0.01		2.68 ± 1.91	1.66 ± 0.10	

DSC = Dice Similarity Coefficient, Ref = References, TRE = Target Registration Error, HD = Hausdorff Distance, MSD = Mean Surface Distance, MEE = Max Estimation Error, PV = Private, CV = Cross-Validation, NM = Not Mentioned, Val = Validation.

MSD: 1.66 ± 0.10 mm, TRE: 2.68 ± 1.91 mm.(See Table 7)

4.2. Discussion

The registration between prostate is an important step in image processing, and the registration between different modal images is an important step in multimodal research. Currently, the main research is the registration between MR images and ultrasound images, and it is mostly used in clinical surgery and treatment, and the registration between MR images and CT images is relatively small. Most of the research in recent years is based on deep learning, and the accuracy has been greatly improved compared with the traditional machine learning registration.

5. Diagnosis of prostate cancer

5.1. Prostate cancer diagnosis based on MR images

In a traditional machine learning algorithm for automatic diagnosis of prostate cancer based on MRI, Giannini et al. [144] used the Otsu algorithm to segment out the prostate region, extract its pharmacokinetic and anatomical features, use a correlation matrix for feature selection, assign 9 features to each voxel, and then use SVM to classify each voxel, creating a malignancy probability map for all voxels of the prostate, then, a candidate segmentation step was performed to highlight suspicious regions to evaluate the number of sensitivity and false positive regions detected by the system. The system had an AUC of 0.91 and a sensitivity of 0.96. Zhang et al. [145] used the improved GrowCut algorithm to segment prostate lesions, used Zernik algorithm for feature extraction, K-nearest neighbor (KNN) algorithm to generate vector model, Multilayer Perceptron (MLP) algorithm to generate network model, and SVM algorithm to generate Beck model. Finally, all the answers will go into a voting system, and their proposed model has an accuracy of 0.8097, a precision of 0.7669, a recall of 0.7732, and an error rate of 0.1902.

The concept of radiomics was proposed by scholars in the Netherlands in 2012. Radiomics is a method to reveal disease characteristics, predict disease progression and treatment effect through digital feature extraction and analysis in medical images. In order to verify the application value of radiomics in prostate cancer detection, Alghoary et al. [146] used the radiomics method to identify whether a patient had clinically significant pre-PCA manifestations. Firstly, the location of adenocarcinoma was drawn by experts, and the features were extracted to screen the top 10 features related to clinically significant tumors by minimum redundancy maximum correlation (mRMR) algorithm. The resulting features are used to train three machine learning classifiers: Quadratic Discriminant Analysis (QDA), Random Forest (RF), SVM. The

results were statistically significant in distinguishing malignant from normal areas. Therefore, radiomics technology can be applied in the detection of prostate cancer, and has a good performance. Following this, Min et al. [147] used an imaging-omics approach to distinguish clinically significant prostate cancer (csPCA) from clinically insignificant prostate cancer (ciPCA). 897 features were extracted from mp-MRI, balanced for minority groups in the training cohort using the SMOTE algorithm, and radiomics features were constructed using the mRMR and LASSO algorithms. Statistical analysis was used to distinguish csPCA from ciPCA. final experimental results AUC, sensitivity, and specificity: 0.823 (95 % CI: 0.669–0.976), 0.841, and 0.727. Abdollahi et al. [148] used Linear Support Vector Machines(LSVM), logistic regression(LREG), Bernoulli's plain Bayes(BENB), Stochastic Gradient Descent(SGD), KNN, Decision Trees(DT), RF, Adaptive augmentation(ADBO), and Gaussian plain Bayes(GANB) to classify patients with GS < 7 and GS > 7. The average AUC for classification of the classification models was 0.739. (See Table 8)

Deep learning is a branch of machine learning, which emerged in 2012. Its powerful performance makes it applied to various fields, and smart medical treatment is one of them. CNN is an important network of deep learning, which is widely used in the field of image processing, and has a large number of applications in the intelligent diagnosis of prostate cancer based on images. Nader et al. [149] proposed a 3D multimodal CNN architecture, which only needs to know the parameters related to lesion centers, with different 3D volume combinations (e.g. ADC, DW, and T2w) as inputs and treats each sequence as a separate input channel; the output is the classification of significant and insignificant lesions. They performed multiple controlled experiments in which the best classification model had an AUC of 0.91, Sensitivity of 0.812, and Specificity of 0.905. Yoo et al. [150] proposed to use CNN to detect clinically significant prostate cancer lesions in patients. DWI was input into five separate pre-trained CNN models for classification, first-order statistical features (such as mean, standard deviation, median, etc.) were extracted from the probability set of CNN output, and important features were selected through a feature selector based on decision trees. Based on these features, RF classifier was used to classify patients into PCa group and non-PCa group. The experiment achieved 0.87(95 % confidence interval (CI): 0.84–0.90) at the slice level and 0.84 (95 % CI: 0.76–0.91) at the patient level.

Transfer learning is an important method in machine learning, which refers to the influence of one kind of learning on another. Applying a pre-trained model to another task can greatly save training time and improve the classification accuracy of the network. Chen et al. [151] proposed a method to improve deep learning network models with transfer learning by performing transfer learning on two pre-trained models (inception v3 and Vgg-16), using the ImageNet [152] dataset pre-trained with inceptionV3 and Vgg-16 models, allowing them to

Table 8

Traditional machine learning methods for prostate cancer diagnosis based on MR images.

Ref	Publication Date	Method	AUC	Sen	Sp	Acc	Pre	Re	Error	Data source	Sample Size (patients)			CV
											Train	Val	Test	
[144]	2015	SVM	0.91	0.96						PV	56	NM	56	Yes
[146]	2018	mRMR,QDA,RF, SVM							0.1902	PV	217	NM	54	No
[147]	2019	mRMR, LASSO algorithm	0.823	0.841	0.727					PV	56	NM	56	No
[148]	2019	LSVM,LREG,BENB, SGD,KNN,DT,ADBO,GANB	0.739							PV	33	NM	33	No
[145]	2021	KNN,SVM,MLP	0.79			0.8097	0.7669	0.7732	0.1902	PV	217	NM	54	No

Sen = Sensitivity, Sp = specificity, Acc = Accuracy, Pre = Precision, Re = Recall, SVM = Support Vector Machine, mRMR = Max-Relevance and Min-Redundancy, QDA = Quadratic Discriminant Analysis, RF = Random Forest, KNN = K-Nearest Neighbor, MLP = Multilayer Perceptron, LSVM = Linear Support Vector Machines, LREG = Logistic Regression, BENB = Bernoulli's plain Bayes, SGD = Stochastic Gradient Descent, DT = Decision Trees, ADBO = Adaptive augmentation, GANB = Gaussian plain Bayes, PV = Private, CV = Cross-Validation, NM = Not Mentioned, Val = Validation.

perform multiple experiments in a limited time. The AUC obtained on the prostateX7 test data were 0.81 and 0.83, respectively. Transfer learning is also introduced. Zhong et al. [153] proposed a deep transfer learning-based model to distinguish between painless and clinically significant prostate cancer lesions. The model uses ResNet network. The T2 SPACE and ADC square image patches that were processed into the surrounding lesions were input into the deep transfer learning-based model to obtain the classification results, and compared with the model without transfer learning. The accuracy for distinguishing painless and clinically significant PCa lesions was 0.723. The sensitivity and specificity were 0.636 and 0.800, respectively. The AUC of the ROC curve was 0.726. The results are better than those without using transfer learning models.

And with the development of deep learning, a variety of novel networks have been proposed and used for the intelligent diagnosis of prostate cancer. Seetharaman et al. [154] created the Stanford Prostate Cancer Network (SPCNet). After training, it can distinguish between aggressive cancer, inert cancer and normal tissue on MRI, T2w and ADC images of prostate cancer regions that have been segmented by experts

are used as input. By using slices containing three adjacent slices, SPCNet includes volume information from adjacent slices when predicting the presence of cancer. SPCNet has an AUC of 0.80–0.81 at the pixel level for detecting normal tissue, 0.64–0.75 for detecting inert tumors, 0.86–0.89 for detecting invasive tumors, and 0.86–0.89 for detecting clinically significant lesions. AUC was 0.75–0.80 for detection of clinically significant lesions. Ye et al. [155] proposed PSP Net + VGG16 based network for segmentation and diagnosis of prostate cancer. The region of interest was segmented using PSP-Net and improved VGG16 was used for prostate cancer and normal prostate classification based on the segmentation effect of PSP Net Dice: 0.913, accuracy and recognition rate based on VGG classification: 0.8795 and 0.8733. Alkadi et al. [49] trained a deep convolutional encoder-decoder architecture to perform both prostate segmentation and diagnosis tasks by giving each voxel a label to perform segmentation of individual regions of the prostate and prostate cancer while identifying prostate cancer lesions. For the cancer detection and localization task, the system has an average AUC of 0.995, an accuracy of 0.894, and a recall of 0.928. (See Table 9)

Table 9

Deep learning methods for prostate cancer diagnosis based on MR images.

Ref	Publication Date	Method	AUC	Sen	Sp	Acc	Pre	Re	Data source	Sample Size (patients)			CV
										Train	Val	Test	
[151]	2017	Transfer learning, Vgg-16,inceptionV3	0.81 (inceptionV3) 0.83 (Vgg-16)						ProstateX	330	NM	208	k-fold
[49]	2018	Deep Convolutional Decoder encoder architecture	0.995			0.894		0.928	I2CVB	1413 (images)	236 (images)	707 (images)	10-fold
[153]	2019	ResNet,Transfer learning	0.711	0.864	0.480	0.660			PV	110	NM	30	No
[149]	2019	multi-channel CNN	0.91	0.812	0.905				PROSTATEX	175	NM	25	No
[150]	2019	CNN,RF	0.87(Slice-level) 0.84 (patient-level)						PV	319	NM	108	No
[154]	2021	SPC-Net	normal tissue:0.8–0.81 indolent cancer:0.64–0.75 aggressive cancer:0.86–0.89 clinically significant lesions: 0.75–0.80						PV	102	NM	29	No
[155]	2022	PSP-Net,Vgg-16	0.87			0.8795	0.8733	0.8973	PV	50	NM	20	No

Sen = Sensitivity, Sp = Specificity, Acc = Accuracy, Pre = Precision, Re = Recall, RF = Random forest, CNN = Convolutional neural network, mRMR = Max-Relevance and Min-Redundancy, PV = Private, CV = Cross-Validation, NM = Not Mentioned, Val = Validation.

5.2. Diagnosis of prostate cancer based on CT images

CT, has the advantages of high resolution imaging, fast imaging, multilevel imaging, with image reconstruction, and is widely used in medicine. In a traditional machine learning approach to diagnose lower prostate cancer using conventional machine learning, Mende et al. [156] used images from External Beam Radiotherapy Treatment, lesion regions delineated by experts, feature extraction using PyRadiomics and LIFEx, and an OvR multi-class strategy classifier based on SVM to obtain the desired results. The image-omics-based approach has also been widely used in the detection of prostate cancer using CT images. Yi et al. [157] used an imagingomics approach to predict the feasibility of intraprostatic lesions not visible on 68 Ga-PSMA-11 PET images in patients with primary prostate cancer. They proposed a machine learning-based radiological model that can derive features from PSMA-PET images to evaluate its effectiveness for lesion prediction. Three sets of features were extracted from standard PET images, delayed PET images, and standard and delayed PET, and the mRMR algorithm was used to filter them, and the filtered features were input into three random forest models, respectively. The average AUC of the three random forest models were 0.87, 0.86, and 0.91, respectively. Osman et al. [158] similarly used an imagingomics approach with one observer to examine and adjust out the prostate structures, using RadiomiX software to extract 1618 radiographic features from each patient's prostate structures. Feature selection was performed using the function find Correlation in the R package, and classification was performed using LASSO and ElasticNet. The classifier was particularly accurate in distinguishing high-risk from low-risk patients and in classifying GS 7 with GS > 7 and GS 7(3+4) with G7(4+3); AUC = 0.9 for classifying GS ≤ 6 and GS ≥ 7, and AUC = 0.98 in classifying GS7(4 + 3) and GS(3 + 4), AUC = 0.96 in distinguishing low risk group from high risk group, AUC = 1.00 in distinguishing low risk group from medium risk group, and AUC = 0.69 in observing GS = 7 and GS > 7. Rustam et al. [159] used naive Bayes and support vector machines to classify prostate cancer by feeding a dataset of CT scans into the SVM and naive Bayes classifiers, respectively. SVM accuracy: 0.8333, naive Bayes accuracy: 0.814.

After the rise of deep learning, Zhong et al. [160] proposed a whole-body training strategy to deal with systemic prostate cancer lesions, which can balance the use of other images without damage to complement the whole-body information. The strategy defines a whole-body scale factor α to determine the ratio of the number of images containing lesions to the number of whole-body images in the training set. While the network model is based on a modification of the U-Net network by changing the input of the model to dual channel (PET/CT) and replacing the U-Net encoder with RegNet, the final lesion results are obtained based on the segmentation results of the network. Precision, Recall and F1-score of 0.829, 1 and 0.906, respectively, were obtained on the independent test set. (See Table 10)

5.3. Prostate cancer diagnosis based on ultrasound images

Ultrasound imaging is an imaging technique based on the physical properties of ultrasound and the parameters of human histology. During medical auxiliary diagnosis, ultrasound technology is often the preferred method of imaging examination [161,162].

Feng et al. [163] used ultrasound features and clinical data to predict the risk of prostate cancer, and input the selected features and clinical data into five machine learning models (decision tree, logistic regression, Bayesian, k-nearest neighbor, support vector machine). Among them, the Bayesian classification effect was the best, with AUC: 0.9278, and the K-nearest neighbor was also high, with AUC: 0.907. Logistic regression was the smallest with an AUC of 0.707. Yang [164] proposed a computer-aided diagnostic system that can distinguish the benign and malignant nature of the lesion area. He proposed an adaptive speckle suppression algorithm based on an improved anisotropic diffusion equation to preprocess rectal ultrasound images, and a fully automated prostate boundary contour segmentation algorithm based on an improved geodesic model. The extraction of feature parameters in the paper includes wavelet domain features, boundary frequency features, spatial gradient features, GLDV features, and the use of a feature dimensional approximate reduction algorithm to select the optimal. The feature dimension reduction algorithm is used to select the optimal subset of feature parameters. The SVM and Adaboost algorithms were used to classify the benign and malignant lesion regions based on the obtained features, where the SVM algorithm using boundary frequency features had the best classification sensitivity: 0.84, specificity: 1, and accuracy: 0.9215. In the same year, Yang et al. [165] proposed to extract features by wavelet transform, extracting wavelet transform texture features and boundary frequency features of the target region in prostate rectal ultrasound images, and selecting the extracted texture features by principal components analysis (PCA) to obtain an optimal subset of features. The K-mean clustering, SVM and AdaBoost (adaptive boosting) algorithms were then applied to classify the extracted texture features of the lesion area. Both the AdaBoost and SVM algorithms can effectively identify the lesion areas with a correct recognition rate of 0.9412 and 0.9346 (See Table 11).

Deep learning is also applied to diagnose prostate cancer from ultrasound images, and Liu et al. [166] used S-Mask R-CNN to segment the prostate, Inception-v3 to detect the lesion, sobel operator to preprocess the image to enhance the prostate boundary, ResNet101 + FPN to extract features to get the feature map, and Region Proposal Network to predict the prostate foreground and The background, the end convolution layer of the prostate ultrasound image is deconvoluted and upsampled using FCN to obtain the segmentation results. The segmentation results are input into Inception-v3 for classification. The original model of Inception is trained using a large amount of data from ImageNet to improve the feature extraction capability of the model, and

Table 10

Machine learning methods for prostate cancer diagnosis based CT images.

Ref	Publication Date	Method	AUC	Sen	SP	Acc	Pre	Re	Data source	Sample Size (patients)			CV
										Train	Val	Test	
[158]	2019	ElasticNet, LASSO	GS ≤ 6 vs. GS ≥ 7:0.83 GS = 7(3 + 4) vs. GS = 7(4 + 3):0.98						PV	342	NM	342	Yes
[156]	2021	SVM,OvR classifier	0.88						PV	44	NM	44	No
[157]	2022	mRMR,RF	0.9925	0.85	0.885	0.870			PV	306	NM	306	No
[159]	2022	Naive Bayes, SVM				Bayes:0.814			PV	166	NM	19	No
[160]	2022	CNN				SVM:0.8333	0.829	100 %	PV	NM	NM	5-fold	

Sen = Sensitivity, Sp = Specificity, Acc = Accuracy, Pre = Precision, Re = Recall, OvR = One-vs-Rest, SVM = Support Vector Machine, CNN = Convolutional Neural Networks, PV = Private, CV = Cross-Validation, NM = Not Mentioned, Val = Validation.

Table 11
Machine learning methods for prostate cancer diagnosis based on Ultrasound images.

Ref	Year	Method	AUC	Sen	Sp	Acc	Pre	Re	Data source	Sample Size(patients)		CV	
										Train	Val		
[164]	2009	SVM,AdaBoost	SVM:0.9475 AdaBoost:0.9416	SVM:0.933 AdaBoost:0.96	SVM:0.962 K-means:0.895	SVM:0.9346 K-means:0.939	SVM:0.9231 SVM:0.933	SVM:0.9412 K-means:0.9176	PV	204	NM	51	5-fold
[165]	2009	K-means,SVM, AdaBoost							PV	204	NM	51	5-fold
[167]	2019	3D-CNN	0.9018 ± 0.0662	0.8298 ± 0.0623	0.9145 ± 0.06				PV	4958 (images)	9372 (images)	7511 (images)	No
[166]	2021	S- Mask R-CNN							PV	422 (images)	140 (images)	140 (images)	No
[163]	2022	DT,KNN,Bayesian network, SVM,LR							PV	178 NM	20 NM	20 10-fold	

Sen = Sensitivity, Sp = Specificity, Acc = Accuracy, Pre = Precision, Re = Recall, SVM = Support Vector Machine, DT = Decision Trees, KNN = K-Nearest Neighbor, LR = Logistic Regression, PV = Private,CV = Cross-Validation, NM = Not Mentioned,Val = Validation.

the classification algorithm uses a gradient descent approach. Its classified benign lesions have a Precision of 0.76, Recall of 0.91, and F1-score of 0.83, and malignant lesions have a Precision of 0.80, Recall of 0.55, and F1-score of 0.65. And with the development of ultrasound technology, techniques such as ultrasonography and time-enhanced ultrasound have emerged. The diagnostic accuracy of prostate cancer has been further improved. For the detection of prostate cancer in ultrasonography images, Feng et al. [167] proposed a deep learning framework for detecting prostate cancer in continuous CEUS, where the original data was a 505×246 AVI video, ten consecutive frames were taken and reconstructed into a set of $23 * 23 * 10$ image tensor, and used 3D-CNN network to automatically detect classified cancer with AUC: 0.9018 ± 0.0662 , sensitivity: 0.8298 ± 0.0623 , and specificity: 0.9145 ± 0.06 .

5.4. Prostate cancer diagnosis based on multimodal approach

Multimodal learning, which aims to give computers the ability to process information from different sources, is used in a number of fields, and is also applied to medical image processing. In using multimodal diagnosis of prostate cancer, Yi et al. [168] develop a computer-assisted diagnosis of prostate cancer, i.e., a prostate cancer localization network and an integrated multimodal classification network, to automatically localize prostate cancer on multiparametric magnetic resonance imaging (mp-MRI) and to classify prostate cancer and noncancerous tissues. The system uses improved V-Net to localize abnormal lesions and proposes two multimodal classification frameworks based on the light-weight architecture [169] of inception-v3 with VGG network Input tensor multi-modal classification network structure and Integrated multi modal classification network structure, in which the classification framework Integrated multi-modal classification network structure has better performance, evaluation index TPR: 0.95, TNR: 0.82, F1- score: 0.8920, AUC: 0.912, Accuracy: 0.885. Yesid et al. [170] proposed a deep multimodal learning framework that models the images of each sequence of MRI individually on separate convolutions to obtain a spatial representation of the better observed texture, then integrates each deep modal branch with inception-like modules to obtain a nonlinear joint representation of the prostate lesion in MP-MRI, and finally flattens the fused representation into embedded vector and mapped to a probability distribution. The experiment takes into account the vascular features in the tumor and correlates the images and in multiple experiments it was found that the sequence containing vascular features (Ktrans) had the best diagnostic performance in combination with the ADC sequence with an AUC of 0.82. Yang et al. [171] used two deep convolutional networks with a single-stage SVM classifier to detect and localize prostate cancer. The two deep convolutional networks were fed with labeled ADC and T2W prostate images and learned the features, respectively. The last convolutional layer of the network explicitly generates a cancer response map for each modality where each pixel denotes the likelihood of a cancer, and the CNN features for each modality were fed into the SVM, and for images classified as containing cancer, the corresponding cancer response map is used for PCa lesion localization using non-maximal suppression and adaptive thresholding methods. The localization and classification of cancer is completed. The AUC for classification is 0.99 and the sensitivity is up to 0.97.

As can be seen from Table 12, the use of multimodal techniques significantly improves the performance of prostate cancer diagnostic models relative to studies that do not use multimodal methods see Table However, current studies of multimodality have focused on multimodality between different sequences using multiparametric magnetic resonance images, and little research has been done on multimodality between different imaging modalities, or between images and cases.

5.5. Discussion

The use of computer-aided diagnosis of prostate cancer can greatly

Table 12

Multimodal learning methods for prostate cancer diagnosis and Typical methods of diagnosing prostate cancer.

Ref	Year	Method	AUC	Sen	Sp	Acc	Pre	Re	Data source	Sample Size (patients)			CV
										Train	Val	Test	
[171]	2017	Two-parallel CNN + SVM	0.99	0.97					PV	NM	NM	NM	NM
[168]	2022	V-Net + inception-v3 and VGG network	0.912			0.885			PROSTAREx	204	NM	104	NM
[170]	2022	Deep Multimodal Learning Framework	0.82						PROSTAREx	320	NM	208	8-fold
[147]	2019	mRMR, LASSO algorithm	0.823	0.841	0.727				PV	56	NM	56	No
[149]	2019	multi-channel CNN	0.91	0.812	0.905				PROSTAREx	175	NM	25	No
[155]	2022	PSP-Net,Vgg-16	0.87			0.8795	0.8733	0.8973	PV	50	NM	20	No

Sen = Sensitivity, Sp = Specificity, Acc = Accuracy, Pre = Precision, Re = Recall, PV = Private,CV = Cross-Validation, NM = Not Mentioned, Val = Validation.

improve the accuracy of diagnosis and reduce the workload of physicians. Most of the current research on prostate cancer diagnosis is based on MR images, and much less research is done on CT images. Currently, deep learning is the mainstream method to diagnose prostate cancer, and the performance index is much improved compared to traditional machine learning methods. However, again, most of the studies are based on MR images, and few studies have used deep learning on CT images to diagnose prostate cancer.

6. Quality assessment

This paper collects and organizes the studies related to prostate cancer on different types of medical images which include preprocessing, segmentation, alignment, and diagnosis of prostate images. Since the studies involve different types of medical images with different research tasks, it is difficult to distinguish their advantages and disadvantages. Therefore, this paper refers to the scoring system in [177], combined with the IJMEDI checklist [178], where two reviewers (Chen and Wu) independently scored the machine learning methods mentioned in this paper. A total of 72 papers were scored. Based on the six dimensions provided in the IJMEDI checklist: problem understanding, data understanding, data modeling, data preparation, modeling, validation, and deployment, a total of 30 questions were asked. Based on the scoring criteria in [177], for high priority items, OK, mR, and MR were scored 2, 1, and 0, respectively. For low priority items, OK, mR, and MR are scored 1, 0.5, and 0, respectively. For scoring options with different viewpoints, the verdict was coordinated by Dr. Liu. The scoring results are shown in Tables 12–16.

Combined with Tables 12–17, it can be found that in the current scoring of the dimensions of imaging-based studies related to prostate cancer, the basic Modeling has always maintained a perfect score, but the Deployment has always been scored low, and by analyzing the papers scored, it can be found that the current research on prostate cancer-related studies is still focused on algorithm improvement and method innovation to improve the prostate-related studies' indicators, but not

on the deployment of related research. Also, since the prostate-related studies collected in this paper are based on medical images to be analyzed, the quality of images collected for studies on different medical images is also different, such as the quality of images collected for studies on prostate on MR is higher than that of CT images and ultrasound images. Meanwhile, current studies rarely perform external validation, which makes it difficult to assess the generalizability of the model. Therefore, the next researchers should pay more attention to the management of the data, with detailed descriptions of the data sources and data descriptions. At the same time, the proposed model should be validated with external datasets to illustrate the generalizability of the model.

Fig. 7 is a line graph of the median total score for each method for this time period based on the time of publication, from which it can be seen that the methods included are generally upwards, in line with the perception.

7. Deficiency and prospect

With the development of machine learning, especially the rise of deep learning. Computers have a wider application in aiding prostate cancer diagnosis research, but at the same time, the following shortcomings still exist:

- (1) Small dataset of annotated images of prostate cancer and poor image quality.

For the problem of small data size, by compiling the literature, we found that there have been methods such as horizontal transformation, adding noise and GAN network to generate images, but there are few applications on prostate. Therefore, the next research can use more GAN and its variants to enhance the data. In addition, other image generation networks can be applied in prostate image generation, such as VAE [172], diffusion model [173], etc. In addition to using data augmentation methods, the training set can be expanded by federal learning. Each

Table 13

Quality assessment scores of the MRI segmentation studies according to the IJMEDI checklist.

Ref	Problem Understanding(10)	Data Understanding(6)	Data Preparation(8)	Modeling(6)	Validation(12)	Deployment(8)	Total(50)
[77]	6	4	2	5	6	1	24
[78]	6	4	2	6	6	2	26
[79]	6	4	7	6	5	1	29
[81]	5	4	3	6	4	2.5	24.5
[19]	7	5	3	6	5	2.5	28.5
[80]	7	4	2	6	6	2.5	27.5
[92]	7	3	6	6	9	3	34
[86]	6	4	4	6	9.5	1.5	31
[20]	5	4	4	6	7	1	27
[85]	8	4	5	6	10	0.5	33.5
[84]	9	4	5	6	7	2	33
[83]	9	4	5	6	8	0.5	32.5
[87]	8	4	0	6	9	0.5	27.5
[93]	9	4	4	6	11	0.5	34.5
[91]	10	4	5	6	7	2	34

Table 14

Quality assessment scores of the CT segmentation studies according to the IJMEDI checklist.

Ref	Problem Understanding(10)	Data Understanding(6)	Data Preparation(8)	Modeling(6)	Validation(12)	Deployment(8)	Total(50)
[100]	4	3	4	6	4	1	22
[96]	6	5	5	6	8	1	31
[99]	5	4	3	6	8	1	27
[97]	5	4	6	4	7	1	27
[98]	8	4	6	6	6	1	31
[101]	7	4	5	6	9	1	32
[95]	5	3	3	6	6	1.5	24.5
[103]	7	3	5	6	7	1	29
[76]	6	3	4	6	8	1.5	28.5
[105]	7	3	2	6	7	1	26
[104]	9	3	2	6	7	1	28
[102]	7	3	4	6	8	0.5	28.5

Table 15

Quality assessment scores of the Ultrasound segmentation studies according to the IJMEDI checklist.

Ref	Problem Understanding(10)	Data Understanding(6)	Data Preparation(8)	Modeling(6)	Validation(12)	Deployment(8)	Total(50)
[113]	7	3	3	6	6	1	26
[109]	7	3	4	6	6	1	27
[106]	4	2	6	6	4	1	23
[107]	7	4	4	6	5	2	28
[112]	4	3	5	6	8	1	27
[108]	5	3	4	6	8	1	27
[111]	7	3	5	6	8	1	30
[110]	5	2	3	6	7	1	24
[115]	7	2	5	6	6	0.5	26.5
[116]	5	2	5	6	6	0.5	24.5
[114]	6	2	4	6	8	0	26
[117]	7	2	3	6	8	0	26
[118]	6	2	3	6	6	0	23

Table 16

Quality assessment scores of the Registration studies according to the IJMEDI checklist.

Ref	Problem Understanding(10)	Data Understanding(6)	Data Preparation(8)	Modeling(6)	Validation(12)	Deployment(8)	Total(50)
[123]	4	2	3	6	4	2	21
[124]	4	4	4	6	6	2	26
[125]	8	4	3	6	8	1	30
[126]	8	4	3	6	7	0	28
[130]	6	2	2	6	7	0	23
[127]	7	4	4	6	8	0	29
[129]	4	1	1	6	2	0	14
[122]	4	4	5	6	6	1	26
[128]	8	3	3	6	8	1	29
[132]	8	3	5	6	8	1	31

hospital trains the models locally, uploads the trained model parameters to the cloud, and the cloud aggregates all the models and returns the aggregated results to the user to improve the accuracy of the models. Since there are multiple types of medical images, in order to expand the data volume, other images can be transformed to the trained image type (e.g., MRI images are transformed to CT images and trained to segment CT images) or the information on other types of images is used to guide the task on that image (e.g., the segmentation model trained using MRI images is used to segment CT images using migration learning methods).

The main approach to the problem of poor image quality is noise reduction. There have been many studies on medical image noise reduction, both traditional machine learning and deep learning, which have good noise reduction performance, but there are not many studies on deep learning for noise reduction on prostate images, and next we can study the application of deep learning methods to noise reduction on prostate images to improve the image quality, such as Eformer [174], CBDNet [175], RIDNet [176] and other networks.

(2) Most of the prostate segmentation studies are overall segmentation, but there are fewer studies on prostate partitioning and the segmentation performance is not satisfying.

Prostate cancer usually occurs in the peripheral and migratory zones, therefore, for the diagnosis of prostate cancer, accurate segmentation of the prostate gland can effectively improve the accuracy of diagnosis. However, most of the studies that exist today segment the prostate as a whole.

The accuracy of segmentation for prostate partitioning is low, and the segmented DSC is mostly around 0.8. Therefore, the next step is to study the segmentation method of the prostate gland to improve the segmentation accuracy to improve the accuracy of prostate cancer diagnosis.

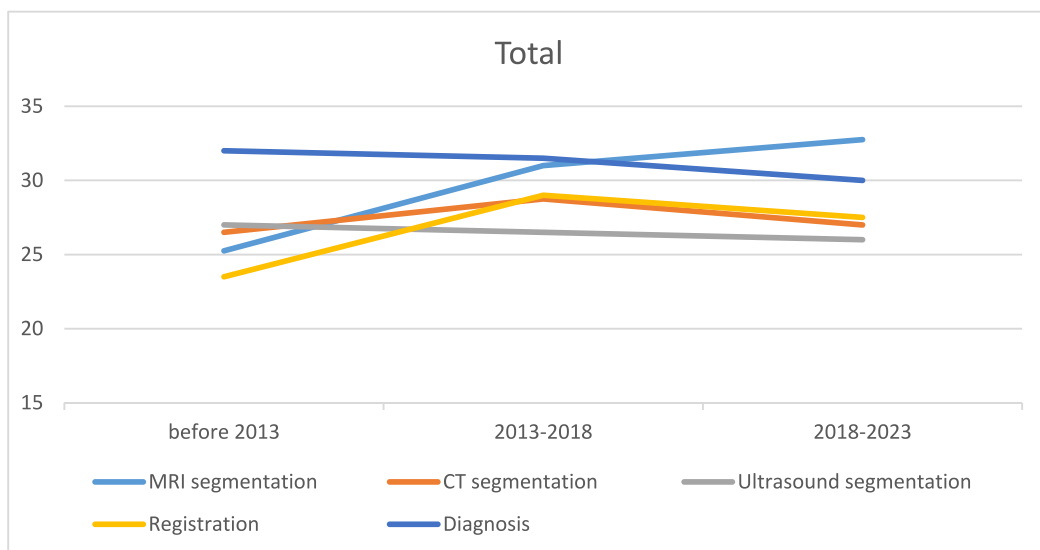
(3) The current research on prostate cancer diagnosis is mostly based on MR images, and there is little research on CT images.

Whether it is traditional machine learning or deep learning, the research on prostate cancer is mostly based on MR images, and there is

Table 17

Quality assessment scores of the Diagnosis studies according to the IJMEDI checklist.

Ref	Problem Understanding(10)	Data Understanding(6)	Data Preparation(8)	Modeling(6)	Validation(12)	Deployment(8)	Total(50)
[135]	9	4	6	6	8	1	34
[137]	8	5	4	6	8	1	32
[138]	7	6	6	6	8	1	34
[139]	8	6	4	6	8	1	33
[136]	4	3	3	6	8	1	25
[141]	5	3	5	6	8	1	28
[39]	8	5	4	6	8	0	31
[143]	9	6	6	6	8	0	35
[140]	9	3	4	6	7	1	30
[114]	8	3	5	6	8	0	30
[144]	7	2	4	6	7	0	26
[145]	5	3	3	6	9	0	26
[148]	4	3	4	6	8	0	25
[146]	7	3	5	6	7	1	29
[147]	7	4	5	6	8	1	31
[149]	7	4	5	5	8	1	30
[150]	7	4	7	3	7	1	29
[152]	7	4	7	6	7	1	32
[153]	7	4	6	6	8	1	32
[155]	9	3	5	6	8	0	31
[154]	9	3	5	6	8	0	31
[151]	10	5	4	6	6	0	31
[168]	10	5	4	6	7	0	32
[170]	9	5	4	5	6	0	29
[171]	7	5	5	6	7	0	30

**Fig. 7.** Median assessment scores according to time of publication.

little research on CT images, especially the research on deep learning applied to diagnose prostate cancer on CT images, to rewrite this sentence CT images to diagnose prostate cancer on CT images.

(4) MR examinations are expensive and cannot be used to observe the patient's lesions all the time.

Due to the high price of MR examination, it is difficult to observe the subsequent changes of prostate cancer in patients through MR examination. Therefore, it is more possible to diagnose prostate cancer and stage prostate cancer by ultrasound images or CT images, and most of the current studies are on prostate cancer diagnosis. MR images are usually valid for one month, while ultrasound images are available in real time, so the next step is to combine MR and ultrasound images to detect and stage the patient's lesions.

(5) A single medical image contains less information and better results can be obtained using multiple types of images to guide studies on the prostate.

Because many different types of images exist in medical imaging, a single image contains limited information. Multimodal approaches can be introduced in subsequent studies. The current existence of multimodal images based on prostate cancer diagnosis is mostly multimodal in a small class within a large class, such as TRUS, ultrasonography and shear wave elastography in ultrasound studies. Multimodality between different diagnostic images is almost absent. Therefore, multimodality studies between different types of medical images can be attempted to improve the diagnostic accuracy (e.g. MRI-ultrasound images, MRI-CT images, CT images-ultrasound images).

8. Conclusion

In recent years, the rapid development of smart medicine has brought new opportunities for prostate cancer diagnosis, and a large number of new imaging methods, new machine learning algorithms, and neural network models have been proposed and applied to related fields. Many studies on the use of computer-aided prostate cancer diagnosis have existed. In this paper, medical image processing is divided into four major categories according to the steps used: pre-processing of prostate images, segmentation of prostate images, registration between different modalities of prostate, and detection and classification of prostate cancer lesions. Also, its study on MR images, CT images, and ultrasound images is detailed according to the different medical images used.

Based on the compiled literature, there are fewer studies related to image pre-processing, both in terms of data enhancement and noise reduction, on the prostate. There are fewer studies on image segmentation for partitioning and the accuracy is low. In terms of image registration, most of the studies on registration are between MR images and ultrasound images, and there are fewer studies on registration between CT and ultrasound. In the detection and classification of prostate cancer lesions, the studies are mostly based on MR images, and there are fewer studies on CT images. And the studies are mostly on the diagnosis of prostate cancer, and there are fewer studies on prostate staging. To address these problems, this paper proposes corresponding solutions, such as applying image generation network (VAE, diffusion model) to the generation of prostate images and applying deep learning to the diagnosis of prostate cancer on CT images, etc.

The use of computer-aided diagnosis of prostate cancer can not only reduce the workload of physicians but also improve the accuracy of diagnosis. Computer diagnosis of prostate cancer has not only a research space but also practical applications.

Author Statement:

Xinyi Chen: The lead author of this paper was responsible for the literature review, data collection and organization, writing the introduction, methods and discussion sections of the paper, and participating in the analysis and revision of the results.

Yuke Wu: Provided advice during the finishing phase of the dissertation and provided important guidance and suggestions during the writing phase of the dissertation, and played an important role in the writing and revision of the discussion section.

Zhenglei Wang: Responsible for collecting and organizing imaging datasets for prostate cancer and providing valuable insights in the analysis and discussion of the results, as well as carefully proofreading the content of the paper.

Shuo Hong Wang: Provided valuable advice and input at all stages of the dissertation writing process. Carried out overall responsibility for revising the structure and language of the thesis to ensure overall logical clarity and accuracy of expression.

Xiang Liu: Provided valuable advice and comments at various stages of the paper writing. Has in-depth expertise in the field of machine learning methods and diagnostic imaging and played an important role in the writing and revision of the discussion section.

Declaration of Competing Interest

The authors declare that they have no known competing financial interests or personal relationships that could have appeared to influence the work reported in this paper.

References

- [1] H. Sung, et al., Global cancer statistics 2020: GLOBOCAN estimates of incidence and mortality worldwide for 36 cancers in 185 countries, CA Cancer J. Clin. 71 (3) (2021) 209–249.
- [2] C. Fitzmaurice, et al., Global, regional, and national cancer incidence, mortality, years of life lost, years lived with disability, and disability-adjusted life-years for 32 cancer groups, 1990 to 2015: a systematic analysis for the global burden of disease study, JAMA Oncol. 3 (4) (2017) 524–548.
- [3] R.L. Siegel, K.D. Miller, A. Jemal, Cancer statistics 2018, CA Cancer J. Clin. 68 (1) (2018) 7–30.
- [4] D. Muthuelo, et al., The detection and upgrade rates of prostate adenocarcinoma following transperineal template-guided prostate biopsy—a tertiary referral centre experience, Central Eur. J. Urol. 69 (1) (2016) 42.
- [5] Z. Mai, et al., Comparison of lesions detected and undetected by template-guided transperineal saturation prostate biopsy, BJU Int. 121 (3) (2018) 415–420.
- [6] S. Wang, et al., Computer auxiliary diagnosis technique of detecting cholangiocarcinoma based on medical imaging: A review, Comput. Methods Prog. Biomed. 208 (2021), 106265.
- [7] X. Jiang, The role and value of imaging medicine in clinical medicine, J. Imag. Res. Med. 4 (09) (2020) 61–62.
- [8] W. Baohua, et al., The application of prostate-specific antigen in prostate cancer early detection in Chinese population: a Meta-analysis, China Oncol. 30 (11) (2020) 879–886.
- [9] J. He, et al., The practical implementation of artificial intelligence technologies in medicine, Nat. Med. 25 (1) (2019) 30–36.
- [10] F. Jiang, et al., Artificial intelligence in healthcare: past, present and future, Stroke Vasc. Neurol. 2 (4) (2017).
- [11] K.W. Johnson, et al., Artificial intelligence in cardiology, J. Am. Coll. Cardiol. 71 (23) (2018) 2668–2679.
- [12] X. Liu, et al., Learning to diagnose cirrhosis with liver capsule guided ultrasound image classification, Sensors 17 (1) (2017) 149.
- [13] A. Eklund, et al., Medical image processing on the GPU—Past, present and future, Med. Image Anal. 17 (8) (2013) 1073–1094.
- [14] L. Yi-nan, et al., Deep learning: path to new era of artificial intelligence, J. Military Commun. Technol. (2015) 4.
- [15] A. Kitchen, and J. Seah, *Support vector machines for prostate lesion classification*, in: *Medical Imaging 2017: Computer-Aided Diagnosis*, SPIE, 2017.
- [16] F. Anna, A novel approach for quantification of time-intensity curves in a DCE-MRI image series with an application to prostate cancer, Comput. Biol. Med. 73 (2016) 119–130.
- [17] D.L. Langer, et al., Prostate cancer detection with multi-parametric MRI: Logistic regression analysis of quantitative T2, diffusion-weighted imaging, and dynamic contrast-enhanced MRI, J Magnetic Resonance Imaging: an Official J. Int. Soc. Magnetic Resonance Med. 30 (2) (2009) 327–334.
- [18] Reda, I., et al. A new CNN-based system for early diagnosis of prostate cancer, in: *2018 IEEE 15th International Symposium on Biomedical Imaging (ISBI 2018)*. 20IEEE.
- [19] P. Schelb, et al., Classification of cancer at prostate MRI: deep learning versus clinical PI-RADS assessment, Radiology 293 (3) (2019) 607–617.
- [20] O. Chilali, et al., Gland and zonal segmentation of prostate on T2W MR images, J. Digit. Imaging 29 (2016) 730–736.
- [21] F. Song, F. Qianjin, Prostate MR image segmentation based on deep learning network PSP-NET, Modern Electronics Technique 42 (12) (2019) 148–151.
- [22] S. Yongtao, et al., Ultrasonic prostate segmentation algorithm based on solution-space constraint, Foreign Electr. Measur. Technol. 42 (03) (2023) 36–45.
- [23] De Raad, K., et al. *The effect of preprocessing on convolutional neural networks for medical image segmentation*, in: *2021 IEEE 18th International Symposium on Biomedical Imaging (ISBI)*. 2021. IEEE.
- [24] F. Yi-fan, X. Qi, Z. Wei-ming, Property analysis model of pleural effusion based on standardization of pleural effusion ultrasonic image, Comput. Sci. (2022) 8.
- [25] S.B. Lee, et al., Deep learning-based computed tomography image standardization to improve generalizability of deep learning-based hepatic segmentation, Korean J. Radiol. 24 (4) (2023) 294.
- [26] S. Albert, et al., Comparison of Image Normalization Methods for Multi-Site Deep Learning, Appl. Sci. 13 (15) (2023) 8923.
- [27] D. Park, et al., Importance of CT image normalization in radiomics analysis: prediction of 3-year recurrence-free survival in non-small cell lung cancer, Eur. Radiol. 32 (12) (2022) 8716–8725.
- [28] DeSilvio, T., et al. *Intensity normalization of prostate MRIs using conditional generative adversarial networks for cancer detection*, in: *Medical Imaging 2021: Computer-Aided Diagnosis*. 2021. SPIE.
- [29] I. Goodfellow, et al., *Generative adversarial networks*, Commun. ACM 63 (11) (2020) 139–144.
- [30] X. Yi, E. Walia, P. Babyn, Generative adversarial network in medical imaging: A review, Med. Image Anal. 58 (2019), 101552.
- [31] Chen, H. and P. Cao. *Deep learning based data augmentation and classification for limited medical data learning*, in: *2019 IEEE international conference on power, intelligent computing and systems (ICPICS)*. 2019. IEEE.
- [32] Deepak, S. and P. Ameer. *MSG-GAN based synthesis of brain MRI with meningioma for data augmentation*, in: *2020 IEEE international conference on electronics, computing and communication technologies (CONECCT)*. 2020. IEEE.
- [33] S. Motamed, P. Rogalla, F. Khalvati, Data augmentation using Generative Adversarial Networks (GANs) for GAN-based detection of Pneumonia and COVID-19 in chest X-ray images, Inf. Med. Unlocked 27 (2021), 100779.
- [34] C. Ge, et al. *Cross-modality augmentation of brain MR images using a novel pairwise generative adversarial network for enhanced glioma classification*, in: *2019 IEEE international conference on image processing (ICIP)*. 2019. IEEE.
- [35] P., Zhuang, A.G. Schwung, and O. Koyejo. *Fmri data augmentation via synthesis*, in: *2019 IEEE 16th International Symposium on Biomedical Imaging (ISBI 2019)*, 2019, IEEE.
- [36] S.B. Alam, and S. Kobashi, Comprehensive modeling of neonatal brain image generation for disorder development onset prediction based on generative

- adversarial networks. Multidisciplinary Computational Anatomy: Toward Integration of Artificial Intelligence with MCA-based Medicine, 2022, p. 269–273.
- [37] A. Segato, et al., Data augmentation of 3D brain environment using deep convolutional refined auto-encoding alpha GAN, *IEEE Transact. Med. Robot. Bionics* 3 (1) (2020) 269–272.
- [38] A. Diaz-Pinto, et al., Retinal image synthesis and semi-supervised learning for glaucoma assessment, *IEEE Trans. Med. Imaging* 38 (9) (2019) 2211–2218.
- [39] M. Nishio, et al., Attribute-guided image generation of three-dimensional computed tomography images of lung nodules using a generative adversarial network, *Comput. Biol. Med.* 126 (2020), 104032.
- [40] H. Yu, X. Zhang, Synthesis of prostate MR images for classification using capsule network-based GAN Model, *Sensors* 20 (20) (2020) 5736.
- [41] I.R. Xu, et al., Generative adversarial networks can create high quality artificial prostate cancer magnetic resonance images, *J. Personal. Med.* 13 (3) (2023) 547.
- [42] J. Ho, A. Jain, P. Abbeel, Denoising diffusion probabilistic models, *Adv. Neural Inf. Proces. Syst.* 33 (2020) 6840–6851.
- [43] W.H. Pinaya, et al., Brain imaging generation with latent diffusion models. *MICCAI Workshop on Deep Generative Models*, Springer, 2022.
- [44] G. Müller-Franzese, et al., Diffusion probabilistic models beat gans on medical images, *arXiv preprint arXiv:075012022*.
- [45] S. Pereira, et al., Brain tumor segmentation using convolutional neural networks in MRI images, *IEEE Trans. Med. Imaging* 35 (5) (2016) 1240–1251.
- [46] Brahim, I., et al. Deep learning methods for MRI brain tumor segmentation: a comparative study, in: *2019 Ninth International Conference on Image Processing Theory, Tools and Applications (IPTA)*, 2019, IEEE.
- [47] S. Afzal, et al., A data augmentation-based framework to handle class imbalance problem for Alzheimer's stage detection, *IEEE Access* 7 (2019) 115528–115539.
- [48] X. Liu, et al., A clinical decision support system for predicting cirrhosis stages via high frequency ultrasound images, *Expert Syst. Appl.* 175 (2021), 114680.
- [49] R. Alkadi, et al., A deep learning-based approach for the detection and localization of prostate cancer in T2 magnetic resonance images, *J. Digit. Imaging* 32 (2019) 793–807.
- [50] Liu, S., et al. *Prostate cancer diagnosis using deep learning with 3D multiparametric MRI*, in: *Medical imaging 2017: computer-aided diagnosis*, 2017, SPIE.
- [51] A. Buades, et al., A review of image denoising algorithms, with a new one, *Multiscale Model. Anal.* 4 (2) (2005) 490–530.
- [52] H. Yu, M. Ding, X. Zhang, Laplacian eigenmaps network-based nonlocal means method for MR image denoising, *Sensors* 19 (13) (2019) 2918.
- [53] J. Hu, et al., Improved DCT-based nonlocal means filter for MR images denoising, *Comput. Mathemat. Methods Med.* 2012 (2012).
- [54] J.V. Manjón, et al., New methods for MRI denoising based on sparseness and self-similarity, *Med. Image Anal.* 16 (1) (2012) 18–27.
- [55] Z. DZ, H. XK, and L. T, Base on improved NL-Means algorithm for medical CT image denoising, *Comput. Tomogr. Theory Applicat.* 22(02) (2013) 297–302.
- [56] J. Yang, et al., Local statistics and non-local mean filter for speckle noise reduction in medical ultrasound image, *Neurocomputing* 195 (2016) 88–95.
- [57] P. Sudeep, et al., Speckle reduction in medical ultrasound images using an unbiased non-local means method, *Biomed. Signal Process. Control* 28 (2016) 1–8.
- [58] G.V. Kumar, M.I. Bellary, T.B. Reddy, Prostate cancer classification with MRI using Taylor-bird squirrel optimization based deep recurrent neural network, *Imag. Sci. J.* 70 (4) (2022) 214–227.
- [59] J.B. Weaver, et al., Filtering noise from images with wavelet transforms, *Magn. Reson. Med.* 21 (2) (1991) 288–295.
- [60] M. Juneja, et al., Denoising of magnetic resonance imaging using Bayes shrinkage based fused wavelet transform and autoencoder based deep learning approach, *Biomed. Signal Process. Control* 69 (2021), 102844.
- [61] C. Cai, et al., Altered patterns of phase position connectivity in default mode subnetwork of subjective cognitive decline and amnestic mild cognitive impairment, *Front. Neurosci.* 14 (2020) 185.
- [62] G. Wang, et al., Asymptomatic COVID-19 CT image denoising method based on wavelet transform combined with improved PSO, *Biomed. Signal Process. Control* 76 (2022), 103707.
- [63] L. Gabralla, H. Mahersia, M. Zaroug, Denoising CT Images using wavelet transform, *Int. J. Adv. Comput. Sci. Applicat.* 6 (5) (2015) 125–129.
- [64] M. Olfa, K. Nawres, Ultrasound image denoising using a combination of bilateral filtering and stationary wavelet transform, *International Image Processing, Applications and Systems Conference*, IEEE, 2014.
- [65] H. Naimi, A.B.H. Adamou-Mitiche, L. Mitiche, Medical image denoising using dual tree complex thresholding wavelet transform and Wiener filter, *J. King Saud University-Comput. Informat. Sci.* 27 (1) (2015) 40–45.
- [66] F. Luisier, T. Blu, P.J. Wolfe, A CURE for noisy magnetic resonance images: Chi-square unbiased risk estimation, *IEEE Trans. Image Process.* 21 (8) (2012) 3454–3466.
- [67] Parthiban, L. and R. Subramanian. *Medical image denoising using X-lets*, in: *2006 Annual IEEE India Conference*, 2006, IEEE.
- [68] A.A. Patil, J. Singhai, Image denoising using curvelet transform: an approach for edge preservation, *J. Sci. Ind. Res.* (2010).
- [69] G. Bhutada, R.S. Anand, S. Saxena, Edge preserved image enhancement using adaptive fusion of images denoised by wavelet and curvelet transform, *Digital Signal Process.* 21 (1) (2011) 118–130.
- [70] K.V. Devarapu, S. Murala, V. Kumar, Denoising of ultrasound images using curvelet transform. 2010 the 2nd International Conference on Computer and Automation Engineering (ICCAE), IEEE, 2010.
- [71] G. Garg, M. Juneja, A survey of denoising techniques for multi-parametric prostate MRI, *Multimedia Tools Applications* 78 (2019) 12689–12722.
- [72] Y. Wang, et al. Reduction of Gibbs artifacts in magnetic resonance imaging based on Convolutional Neural Network, in: *2017 10th international congress on image and signal processing, biomedical engineering and informatics (CISP-BMEI)*. 2017.
- [73] K. Zhang, et al., Beyond a gaussian denoiser: Residual learning of deep cnf for image denoising, *IEEE Trans. Image Process.* 26 (7) (2017) 3142–3155.
- [74] D. Xie, L. Bai, and Z. Wang, *Denoising arterial spin labeling cerebral blood flow images using deep learning*, arXiv preprint arXiv:09672, 2018.
- [75] L. Wu, S. Hu, C. Liu, Denoising of 3D brain MR images with parallel residual learning of convolutional neural network using global and local feature extraction, *Computational Intelligence Neuroscience* 2021 (2021) 1–18.
- [76] D. Hong, et al., FFA-DMRI: A network based on feature fusion and attention mechanism for brain MRI denoising, *Front. Neurosci.* 14 (2020), 577937.
- [77] C. Tian, et al., Attention-guided CNN for image denoising, *Neural Netw.* 124 (2020) 117–129.
- [78] C. Ahn, C. Heo, and J.H. Kim. *Combined low-dose simulation and deep learning for CT denoising: application in ultra-low-dose chest CT*, in: *International forum on medical imaging in Asia 2019*. 2019. SPIE.
- [79] M. Chen, Y.-F. Pu, Y.-C. Bai, A fractional-order variational residual CNN for low dose CT image denoising, *Intelligent Computing Theories and Application: 15th International Conference, ICIC 2019, Nanchang, China, August 3–6, 2019, Proceedings, Part I* 15, Springer, 2019.
- [80] B. Kim, et al., A performance comparison of convolutional neural network-based image denoising methods: The effect of loss functions on low-dose CT images, *Med. Phys.* 46 (9) (2019) 3906–3923.
- [81] H.R. Shahdoost, Z. Rahemi, Edge-preserving image denoising using a deep convolutional neural network, *Signal Process* 159 (2019) 20–32.
- [82] E.A. Kaye, et al., Accelerating prostate diffusion-weighted MRI using a guided denoising convolutional neural network: retrospective feasibility study, *Radiol. Artif. Intell.* 2 (5) (2020) e200007.
- [83] P. Aggarwal, et al., Role of segmentation in medical imaging: A comparative study, *Int. J. Comput. Applicat.* 29 (1) (2011) 54–61.
- [84] A. Balagopal, et al., Fully automated organ segmentation in male pelvic CT images, *Phys. Med. Biol.* 63 (24) (2018), 245015.
- [85] J. Xiong, *Automatic segmentation of the prostate on 3D CT images by using multiple deep learning networks* 2019, Shanghai Jiao Tong University.
- [86] L. Tong, Y. Wanqi, Y. Ming, Prostate segmentation in CT images with multimodal U-net, *CAAI Transact. Intell. Syst.* 13 (6) (2018) 981–988.
- [87] S. Klein, et al., Automatic segmentation of the prostate in 3D MR images by atlas matching using localized mutual information, *Med. Phys.* 35 (4) (2008) 1407–1417.
- [88] X. Liu, et al. Unsupervised segmentation of the prostate using MR images based on level set with a shape prior, in: *2009 Annual International Conference of the IEEE Engineering in Medicine and Biology Society*. 2009. IEEE.
- [89] R. Toth, A. Madabhushi, Multifeature landmark-free active appearance models: application to prostate MRI segmentation, *IEEE Trans. Med. Imaging* 31 (8) (2012) 1638–1650.
- [90] Y. Shi-ju, H. Yong-sen, T. Guang-yu, An improved level set algorithm for prostate region segmentation, *Chinese J. Magn. Reson.* 38 (3) (2021) 356–366.
- [91] D. Mahapatra, J.M. Buhmann, Prostate MRI segmentation using learned semantic knowledge and graph cuts, *IEEE Trans. Biomed. Eng.* 61 (3) (2013) 756–764.
- [92] Y. Zhu, et al., Fully automatic segmentation on prostate MR images based on cascaded fully convolution network, *J. Magn. Reson. Imaging* 49 (4) (2019) 1149–1156.
- [93] M. Bardis, et al., Segmentation of the prostate transition zone and peripheral zone on MR images with deep learning, *Radiol.: Imaging Cancer* 3 (3) (2021) e200024.
- [94] A. Ushinsky, et al., A 3D–2D hybrid U-net convolutional neural network approach to prostate organ segmentation of multiparametric MRI, *Am. J. Roentgenol.* 216 (1) (2021) 111–116.
- [95] S. Motamed, et al., A transfer learning approach for automated segmentation of prostate whole gland and transition zone in diffusion weighted MRI. arXiv preprint arXiv:09541, 2019.
- [96] Z. Tian, et al., PSNet: prostate segmentation on MRI based on a convolutional neural network, *J. Med. Imaging* 5 (2) (2018) 021208.
- [97] R. Cuocolo, et al., Deep learning whole-gland and zonal prostate segmentation on a public MRI dataset, *J. Magn. Reson. Imaging* 54 (2) (2021) 452–459.
- [98] M. Tan, and Q. Le, Efficientnet: Rethinking model scaling for convolutional neural networks, in: *International conference on machine learning*. 2019. PMLR.
- [99] O. Ronneberger, P. Fischer, T. Brox, U-net: Convolutional networks for biomedical image segmentation. *Medical Image Computing and Computer-Assisted Intervention—MICCAI 2015: 18th International Conference, Munich, Germany, October 5–9, 2015, Proceedings, Part III* 18, Springer, 2015.
- [100] E. Romera, et al., Erfnet: Efficient residual factorized convnet for real-time semantic segmentation, *IEEE Trans. Intell. Transp. Syst.* 19 (1) (2017) 263–272.
- [101] L. Xiang, et al., Regional segmentation of prostate and clinical evaluation in T2WI image based on 3D U-Net model, *J. China Clin. Med. Imag.* 33 (01) (2022) 33–38.
- [102] F. Milletari, N. Navab, and S.-A. Ahmadi. V-net: Fully convolutional neural networks for volumetric medical image segmentation, in: *2016 fourth international conference on 3D vision (3DV)*. 2016. Ieee.
- [103] Y. Jin, et al., 3D PBV-Net: an automated prostate MRI data segmentation method, *Comput. Biol. Med.* 128 (2021), 104160.
- [104] G. Litjens, et al., Evaluation of prostate segmentation algorithms for MRI: the PROMISE12 challenge, *Med. Image Anal.* 18 (2) (2014) 359–373.
- [105] A. Kos, J. Bulat, Comparison of ASM and CNN Based Prostate Segmentation in CT Images, IEEE, 2021.

- [106] W. Li, et al., Learning image context for segmentation of prostate in CT-guided radiotherapy. *Medical Image Computing and Computer-Assisted Intervention—MICCAI 2011: 14th International Conference, Toronto, Canada, September 18–22, 2011, Proceedings, Part III* 14, Springer, 2011.
- [107] F. Commandeur, et al. *Segmentation of prostate from CT scans using a combined voxel random forests classification with spherical harmonics regularization*, in: *10th International Symposium on Medical Information Processing and Analysis*, 2015, SPIE.
- [108] L. Ma, et al., A combined learning algorithm for prostate segmentation on 3D CT images, *Med. Phys.* 44 (11) (2017) 5768–5781.
- [109] Y. Shao, et al., CT prostate deformable segmentation by boundary regression. *Medical Computer Vision: Algorithms for Big Data: International Workshop, MCV 2014, Held in Conjunction with MICCAI 2014, Cambridge, MA, USA, September 18, 2014, Revised Selected Papers 4*, Springer, 2014.
- [110] Ghosh, P. and M. Mitchell. *Prostate segmentation on pelvic CT images using a genetic algorithm*, in: *Medical Imaging 2008: Image Processing*. 2008. SPIE.
- [111] M. Shahedi, et al., A semi-automatic segmentation method for prostate in CT images using local texture classification and statistical shape modeling, *Med. Phys.* 45 (6) (2018) 2527–2541.
- [112] K. He, et al., HF-UNet: learning hierarchically inter-task relevance in multi-task U-net for accurate prostate segmentation in CT images, *IEEE Trans. Med. Imaging* 40 (8) (2021) 2118–2128.
- [113] L. Ma, et al. Automatic segmentation of the prostate on CT images using deep learning and multi-atlas fusion, in: *Medical imaging 2017: Image processing*. 2017. SPIE.
- [114] Y. Lei, et al., CT prostate segmentation based on synthetic MRI-aided deep attention fully convolution network, *Med. Phys.* 47 (2) (2020) 530–540.
- [115] J. Xiong, L. Jiang, and Q. Li. Automatic segmentation of the prostate on 3D CT images by using multiple deep learning networks, in: *Proceedings of the 2018 5th International Conference on Biomedical and Bioinformatics Engineering*. 2018.
- [116] F. Sahba, H.R. Tizhoosh, M.M. Salama, Segmentation of Prostate Boundaries Using Regional Contrast Enhancement, *IEEE*, 2005. 2005.
- [117] P. Yan, et al., Discrete deformable model guided by partial active shape model for TRUS image segmentation, *IEEE Trans. Biomed. Eng.* 57 (5) (2010) 1158–1166.
- [118] L. Weiping, Y. Xin, Segmentation of Prostate from Ultrasound Image Using Shape Prior Constraint, *Microcomput. Appl.* 28 (6) (2012) 1–5.
- [119] L. Gong, et al., Parametric shape modeling using deformable superellipses for prostate segmentation, *IEEE Trans. Med. Imaging* 23 (3) (2004) 340–349.
- [120] G. Xiao, et al., Ultrasound image segmentation based on Zernike moment and level set, *J. Southeast University (Nat. Sci. Ed.)* 45 (2) (2015) 247–250.
- [121] H. Jianbo, N. Dong, W. Tianfu, Automatic segmentation method based on probability priors and statistical shape for prostate TRUS images, *J. Biomed. Eng. Res.* 34 (1) (2015) 15–19.
- [122] S. Ghose, et al. *Multiple mean models of statistical shape and probability priors for automatic prostate segmentation*, in: *Prostate Cancer Imaging. Image Analysis and Image-Guided Interventions: International Workshop, Held in Conjunction with MICCAI 2011, Toronto, Canada, September 22, 2011. Proceedings 2*. 2011. Springer.
- [123] W.D. Richard, C.G. Keen, Automated texture-based segmentation of ultrasound images of the prostate, *Comput. Med. Imaging Graph.* 20 (3) (1996) 131–140.
- [124] Y. Lei, et al., Ultrasound prostate segmentation based on multidirectional deeply supervised V-Net, *Med. Phys.* 46 (7) (2019) 3194–3206.
- [125] Y. Wang, et al., Deep attentional features for prostate segmentation in ultrasound. *Medical Image Computing and Computer Assisted Intervention—MICCAI 2018: 21st International Conference, Granada, Spain, September 16–20, 2018, Proceedings, Part IV* 11, Springer, 2018.
- [126] Y. Wang, et al., Deep attentive features for prostate segmentation in 3D transrectal ultrasound, *IEEE Trans. Med. Imaging* 38 (12) (2019) 2768–2778.
- [127] N. Orlando, et al., Automatic prostate segmentation using deep learning on clinically diverse 3D transrectal ultrasound images, *Med. Phys.* 47 (6) (2020) 2413–2426.
- [128] C. Zhijie, Prostate segmentation algorithm based on YOLOv5 and average template, *Changjiang Informat. Communicat.* 36 (02) (2023) 44–47.
- [129] L.G. Brown, A survey of image registration techniques, *ACM Comput. Surv.* 24 (4) (1992) 325–376.
- [130] L. Shuqian, L. Weixue, Medical image registration technology, *Int. J. Biomed. Eng.* 22 (1) (1999) 1–8.
- [131] H.Y. Li, et al., Machine Learning in Prostate MRI for Prostate Cancer. Current Status and Future Opportunities, *Diagnostics* 12 (2) (2022).
- [132] C. Ming, et al., Prostate MR/TRUS image segmentation and registration methods based on supervised learning, *Chinese J. Eng.* 42 (10) (2020) 1362–1371.
- [133] A. Mohamed, C. Davatzikos, and R. Taylor. A combined statistical and biomechanical model for estimation of intra-operative prostate deformation, in: *Medical Image Computing and Computer-Assisted Intervention—MICCAI 2002: 5th International Conference Tokyo, Japan, September 25–28, 2002 Proceedings, Part II* 5. 2002. Springer Berlin Heidelberg.
- [134] Y. Hu, et al., Modelling prostate motion for data fusion during image-guided interventions, *IEEE Trans. Med. Imaging* 30 (11) (2011) 1887–1900.
- [135] Y. Hu, et al., Weakly-supervised convolutional neural networks for multimodal image registration, *Med. Image Anal.* 49 (2018) 1–13.
- [136] P. Yan, et al., Adversarial image registration with application for MR and TRUS image fusion. *Machine Learning in Medical Imaging: 9th International Workshop, MLMI 2018, Held in Conjunction with MICCAI 2018, Granada, Spain, September 16, 2018, Proceedings 9*, Springer, 2018.
- [137] Q. Zeng, et al., Label-driven magnetic resonance imaging (MRI)-transrectal ultrasound (TRUS) registration using weakly supervised learning for MRI-guided prostate radiotherapy, *Phys. Med. Biol.* 65 (13) (2020), 135002.
- [138] Y. Chen, et al., MR to ultrasound image registration with segmentation-based learning for HDR prostate brachytherapy, *Med. Phys.* 48 (6) (2021) 3074–3083.
- [139] X. Yang, et al., Deformable MRI-TRUS registration using biomechanically constrained deep learning model for tumor-targeted prostate brachytherapy, *Int. J. Radiat. Oncol. Biol. Phys.* 108 (3) (2020) e339.
- [140] G. Shafai-Erfani, et al., Dose evaluation of MRI-based synthetic CT generated using a machine learning method for prostate cancer radiotherapy, *Med. Dosim.* 44 (4) (2019) e64–e70.
- [141] Y. Fu, et al., Deformable MR-CBCT prostate registration using biomechanically constrained deep learning networks, *Med. Phys.* 48 (1) (2021) 253–263.
- [142] K.J. Kon, 장윤진, and 조경구, *Multidisciplinary Functional MR Imaging for Prostate Cancer*, Korean J. Radiol. 10 (6) (2009) 535–551.
- [143] S.A. Kwee, M.N. Coel, J. Lim, Detection of recurrent prostate cancer with 18F-fluorocholine PET/CT in relation to PSA level at the time of imaging, *Ann. Nucl. Med.* 26 (6) (2012) 501–507.
- [144] V. Giannini, et al., A fully automatic computer aided diagnosis system for peripheral zone prostate cancer detection using multi-parametric magnetic resonance imaging, *Comput. Med. Imaging Graph.* 46 (2015) 219–226.
- [145] L. Zhang, et al., A new approach to diagnosing prostate cancer through magnetic resonance imaging, *Alex. Eng. J.* 60 (1) (2021) 897–904.
- [146] A. Alghولي, et al., Radiomic features on MRI enable risk categorization of prostate cancer patients on active surveillance: Preliminary findings, *J. Magn. Reson. Imaging* 48 (3) (2018) 818–828.
- [147] X. Min, et al., Multi-parametric MRI-based radiomics signature for discriminating between clinically significant and insignificant prostate cancer: Cross-validation of a machine learning method, *Eur. J. Radiol.* 115 (2019) 16–21.
- [148] H. Abdollahi, et al., Machine learning-based radiomic models to predict intensity-modulated radiation therapy response, Gleason score and stage in prostate cancer, *Radiol. Med.* 124 (2019) 555–567.
- [149] N. Aldoj, et al., Semi-automatic classification of prostate cancer on multi-parametric MR imaging using a multi-channel 3D convolutional neural network, *Eur. Radiol.* 30 (2) (2020) 1243–1253.
- [150] S. Yoo, et al., Prostate cancer detection using deep convolutional neural networks, *Sci. Rep.* 9 (1) (2019) 1–10.
- [151] Q. Chen, et al. A transfer learning approach for classification of clinical significant prostate cancers from mpMRI scans, in: *Medical Imaging 2017: Computer-Aided Diagnosis*. 2017. SPIE.
- [152] J. Deng, et al., Imagenet: A large-scale hierarchical image database. *2009 IEEE Conference on Computer Vision and Pattern Recognition*, Ieee, 2009.
- [153] X. Zhong, et al., Deep transfer learning-based prostate cancer classification using 3 Tesla multi-parametric MRI, *Abdominal Radiology* 44 (2019) 2030–2039.
- [154] A. Seetharaman, et al., Automated detection of aggressive and indolent prostate cancer on magnetic resonance imaging, *Med. Phys.* 48 (6) (2021) 2960–2972.
- [155] L.-Y. Ye, et al., Medical image diagnosis of prostate tumor based on PSP-Net+VGG16 deep learning network, *Comput. Methods Prog. Biomed.* 221 (2022), 106770.
- [156] B. Mendes, et al., Prostate Cancer Aggressiveness Prediction Using CT Images, *Life* 11 (11) (2021) 1164.
- [157] Z. Yi, et al., Machine learning-based prediction of invisible intraprostatic prostate cancer lesions on 68 Ga-PSMA-11 PET/CT in patients with primary prostate cancer, *Eur. J. Nucl. Med. Molecul. Imag.* (2022) 1–12.
- [158] S.O. Osman, et al., Computed tomography-based radiomics for risk stratification in prostate cancer, *Int. J. Radiat. Oncol. Biol. Phys.* 105 (2) (2019) 448–456.
- [159] Z. Rustam, et al., Support vector machines and Naïve Bayes classifier for classifying a prostate cancer, in: *Adv. Intell. Syst. Sustain. Develop. (AI2SD’2020)*, Volume 1, Springer, 2022, pp. 854–860.
- [160] S. Zhong, et al. Automatic Detection of Prostate Cancer Systemic Lesions Based on Deep Learning and 68 Ga-PSMA-11 PET/CT, in: *2022 IEEE 35th International Symposium on Computer-Based Medical Systems (CBMS)*. 2022. IEEE.
- [161] J. Peng, et al., Fabrication and performance of a miniaturized and integrated endoscope ultrasound convex array for digestive tract imaging, *IEEE Trans. Biomed. Eng.* 65 (1) (2017) 140–148.
- [162] Y. Liu, et al., A novel method for accurate extraction of liver capsule and auxiliary diagnosis of liver cirrhosis based on high-frequency ultrasound images, *Comput. Biol. Med.* 125 (2020), 104002.
- [163] F. Yu-jie, et al., The value of machine learning based on ultrasound image features in predicting the risk of prostate cancer, *J. China Clin. Med. Imag.* 33 (01) (2022) 28–32.
- [164] Z. Yang, Computer Aided Diagnosis of Prostate Pathology Based on TRUS Images, *University of Science and Technology of China*, 2009.
- [165] Z. Yang, et al., Diagnosis of Prostate cancer and texture feature extraction of ultrasound images based on wavelet transform, *Space Med. Med. Eng.* 22 (4) (2009) 281–285.
- [166] Z. Liu, et al., Deep learning framework based on integration of S-Mask R-CNN and Inception-v3 for ultrasound image-aided diagnosis of prostate cancer, *Futur. Gener. Comput. Syst.* 114 (2021) 358–367.
- [167] Y. Feng, et al., A deep learning approach for targeted contrast-enhanced ultrasound based prostate cancer detection, *IEEE/ACM Transact. Computat. Biol. Bioinformat.* 16 (6) (2018) 1794–1801.
- [168] Z. Yi, et al., Computer-aided diagnosis of prostate cancer based on deep neural networks from multi-parametric magnetic resonance imaging, *Front. Physiol.* 13 (2022), 918381.
- [169] B. Rueckauer, et al., Conversion of continuous-valued deep networks to efficient event-driven networks for image classification, *Front. Neurosci.* 11 (2017) 682.

- [170] Y. Gutiérrez, J. Arevalo, F. Martínez, An inception-based deep multiparametric net to classify clinical significance MRI regions of prostate cancer, *Phys. Med. Biol.* 67 (22) (2022), 225004.
- [171] X. Yang, et al., Co-trained convolutional neural networks for automated detection of prostate cancer in multi-parametric MRI, *Med. Image Anal.* 42 (2017) 212–227.
- [172] C. Doersch, Tutorial on variational autoencoders. arXiv preprint arXiv:05908, 2016.
- [173] C. Saharia, et al. *Palette: Image-to-image diffusion models.* in: *ACM SIGGRAPH 2022 Conference Proceedings*. 2022.
- [174] A. Luthra, et al., Eformer: Edge enhancement based transformer for medical image denoising. arXiv preprint arXiv:08044, 2021.
- [175] S. Guo, et al. Toward convolutional blind denoising of real photographs, in: *Proceedings of the IEEE/CVF conference on computer vision and pattern recognition*. 2019.
- [176] S. Anwar, and N. Barnes. Real image denoising with feature attention, in: *Proceedings of the IEEE/CVF international conference on computer vision*. 2019.
- [177] Y. Zhou, et al., Machine learning predictive models for acute pancreatitis: A systematic review, *Int. J. Med. Inf.* 157 (2022).
- [178] F. Cabitza, A.J.I.J.o.M.I. Campagner, The need to separate the wheat from the chaff in medical informatics, (2021) 104510. Doi: 10.1016/j.ijmedinf.2021.104510.